

# IGFEM-based Shape Sensitivity Analysis of the Transverse Failure of a Composite Laminate

Xiang Zhang\*; David R. Brandyberry and Philippe H. Geubelle

*Department of Aerospace Engineering, University of Illinois, Urbana, IL, USA*

## Abstract

This manuscript presents a shape sensitivity analysis method based on an Interface-enriched Generalized Finite Element Method (IGFEM) formulation and its application to the sensitivity of the transverse failure of a fiber-reinforced composite laminate with respect to the geometrical parameters that define its microstructure. The analytical sensitivities with respect to individual fiber radius and placement are first derived within the context of a cohesive IGFEM solver specially developed to simulate the fiber/matrix debonding observed in the transverse failure of composite laminates with high fiber volume fraction. The IGFEM solver utilizes  $C^{-1}$  continuous enrichment functions and a cohesive failure model to capture the transverse cracking associated primarily with fiber/matrix interface debonding. In addition to the sensitivities with respect to individual geometrical parameters such as the radius of individual fibers, the sensitivities of the transverse stress-strain response with respect to the parameters that define the distributions of the geometrical parameters such as the mean and standard deviation of the fiber radius and nearest-neighbor distance distributions are also derived. The sensitivity analysis is performed on realistic microstructures composed of hundreds of fibers to characterize the influence of the geometrical parameters and their distributions on the transverse failure response of the composite laminate.

*Keywords:* Fiber-reinforced composite laminate; Transverse failure; Fiber/matrix interface debonding; Shape sensitivity; Cohesive failure model; IGFEM

## 1 Introduction

A recent addition to the family of generalized finite element methods (GFEM), the Interface-enriched GFEM, or IGFEM, has been used to simulate the thermal, structural or electromagnetic response of a variety of heterogeneous materials and structures [1, 2, 3, 4]. Like its

---

\*Corresponding author. Tel.: +1 217 244 7648; Fax: +1 217 244 0720 Email address: zhangx22@illinois.edu (X. Zhang)

GFEM counterparts, the IGFEM relies on finite element discretizations that do not conform to the material microstructures and introduces in the non-conforming elements traversed by the material interfaces an enrichment that captures the essence (e.g., weak or strong discontinuity) of the solution along these interfaces. However, unlike in conventional GFEM where the generalized degrees of freedom associated with the enrichment field are assigned to the nodes of the non-conforming mesh, the additional degrees of freedom in the IGFEM are associated with points located along the material interfaces. More recently, the IGFEM was combined with a shape sensitivity formulation to perform a gradient-based design of actively cooled microvascular composite panels for battery and nanosatellite applications [5, 6, 7, 8, 9], and for the multiscale design of heterogeneous materials [10, 11].

The present manuscript builds on this previous work but focuses on the IGFEM-based extraction of the sensitivity of the interface-driven failure of heterogeneous materials. Emphasis is placed on the failure modeling of materials whose microstructure is composed of a large number of inclusions and is described by a set of randomly distributed shape parameters. The objective of this work is thus to extract the sensitivity of the failure response of the material with respect to the parameters that describe the distribution of the geometrical descriptors (e.g., shape and placement) of the inclusions present in the microstructure.

The particular application investigated in this work pertains to the transverse failure of a composite laminate, which has long been considered as a precursor to more critical failure events such as inter-ply delamination and fiber breakage [12, 13, 14, 15]. The initiation and propagation of transverse cracks are affected by a variety of microstructural quantities including fiber placement, fiber radii, constitutive properties of the fibers and the matrix, as well as the failure properties of the fiber/matrix interfaces. A proper choice of these parameters can lead to improved stress-strain response and increased strain to failure. Therefore, the ability to model transverse cracking in fiber-reinforced composites and calculate the sensitivities of the response of the laminate with respect to relevant microstructural parameters may be valuable tools for the design of better composites.

In a unidirectional ply with high fiber volume fraction under transverse tensile loading, failure typically initiates at the fiber/matrix interfaces and propagates along these interfaces to form cracks spanning the entire  $90^\circ$  ply (Fig. 1). Modeling these interface failures requires a fully resolved microstructure as well as the ability to capture the displacement discontinuities across the interfaces. One attractive approach is the finite-element-based cohesive zone model (CZM) [16, 17], in which fracture is modeled as a gradual process of surface separation resisted by cohesive tractions. CZM is particularly attractive in situations where the potential crack paths are known a priori, such as along material interfaces [18, 19, 20, 21].

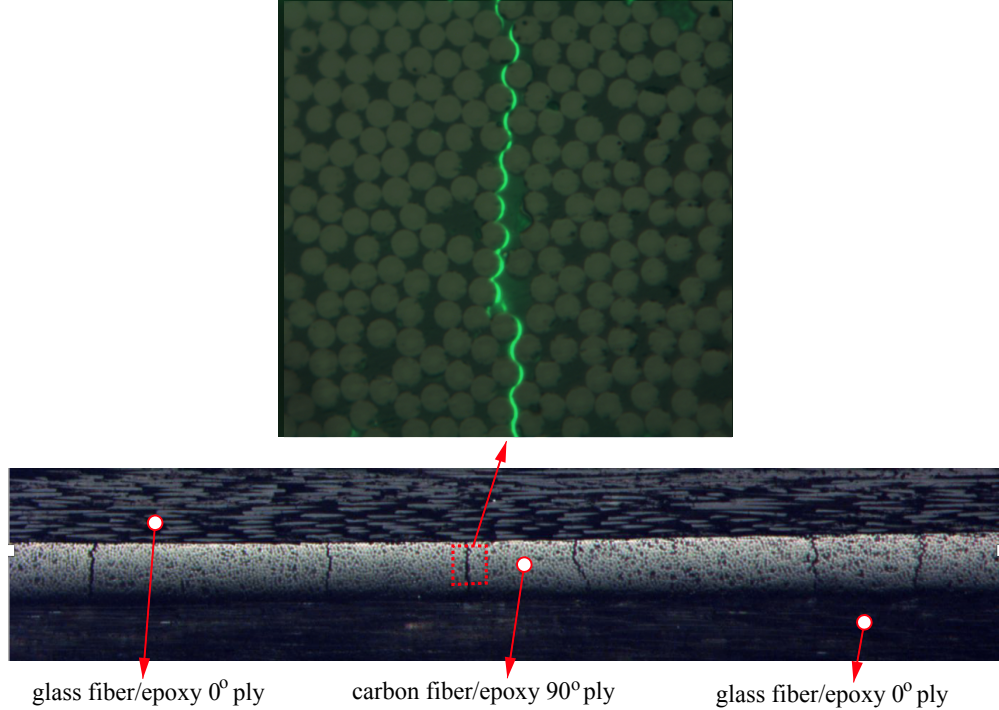


Figure 1: Transverse cracks in the  $90^\circ$  ply of a hybrid  $[0/90/0]_T$  glass/carbon epoxy composite laminate subjected to transverse tensile loading. The top figure shows details of the transverse crack path taking place primarily along fiber/matrix interfaces. The use of glass fibers in the  $0^\circ$  plies allows for the initiation of transverse cracking at a lower load level more readily achievable by the experimental setup described in [22].

To model the fiber/matrix debonding failure we adopt a cohesive form of the IGFEM based on a  $C^{-1}$  enrichment of the solution in the elements traversed by the fiber/matrix interfaces and a cohesive failure model to describe the progressive debonding of these interfaces [23, 24, 25]. The application of the cohesive IGFEM to the problem of interest, i.e., the transverse failure of composite laminate, has been validated by Zacek et al. [26]. It is also the basis of the study conducted by Shakiba et al. [27] who extracted the sensitivities of transverse stress-strain response with respect to the parameters that define the cohesive properties of the fiber/matrix interfaces and their distributions.

As indicated earlier, we focus in this study on the dependence of the transverse failure response of the composite laminate on the geometrical parameters that define the microstructure of the  $90^\circ$  ply. Using an analytical sensitivity method combined with the IGFEM solver, we start by computing the shape sensitivities of the transverse stress-strain response with respect to the radius and placement of individual fibers and verify these sensitivities through a comparison with finite difference approximations. We then use these individual sensitivities to extract the sensitivities of the transverse response on the parameters (mean and standard deviation) that describe the distributions of the fiber radius and nearest-neighbor distance.

The remainder of this manuscript is organized as follows: The sensitivities of the transverse

stress-strain response with respect to the geometrical parameters associated with individual fibers and with respect to the distributions of these parameters are derived within the context of the cohesive IGFEM in Section 2. These analytic sensitivities are verified against finite difference approximations in Section 3, while Section 4 presents a sensitivity analysis performed on a realistic composite microstructure involving hundreds of fibers.

## 2 Shape Sensitivity Analysis

### 2.1 Overview of cohesive IGFEM

As indicated earlier, a cohesive IGFEM formulation based on strongly discontinuous ( $C^{-1}$ ) enrichment functions was recently used by Zacek et al. [26] to model the displacement discontinuity along the debonding fiber/matrix interfaces. The authors also used an image-based microstructure reconstruction method to allow for the mesoscale modeling of transverse cracks in realistic microstructures created directly from optical images of actual composite laminate specimens. For completeness and to introduce the notations used in the sensitivity formulation, we summarize in this section the cohesive IGFEM scheme. For more information, please see Zacek et al. [26] and the references therein. Following the standard discretization procedure, the system of nonlinear equations describing the equilibrium of the 2D domain can be expressed as

$$\mathbf{A}_e \left\{ \int_{\Omega_e} \mathbf{B}^T \boldsymbol{\sigma}(\mathbf{U}, \mathbf{d}) \, dA + \int_{\partial\Omega_e^c} \mathbf{B}_c^T \mathbf{t}_c(\mathbf{U}, \mathbf{d}) \, dS \right\} = \mathbf{A}_e \left\{ \int_{\Omega_e} \mathbf{N}^T \mathbf{b} \, dA + \int_{\partial\Omega_e^t} \mathbf{N}^T \mathbf{s}_t \, dS \right\}, \quad (1)$$

where the vector  $\mathbf{U}$  contains the nodal displacements and the generalized (enrichment) degrees of freedom associated with the elements traversed by the fiber/matrix interfaces, and  $\mathbf{d}$  denotes the vector of geometrical parameters that define the microstructure, i.e., the center coordinates and radius of the  $n$  fibers:  $\mathbf{d} = [x_{c1}, y_{c1}, R_1, x_{c2}, y_{c2}, R_2, \dots, x_{cn}, y_{cn}, R_n]$ .  $\mathbf{A}_e$  denotes the assembly operator, the matrix  $\mathbf{B}$  contains the spatial derivatives of the shape functions,  $\mathbf{B}_c = \mathbf{R}\mathbf{N}_c$  is the global displacement-separation matrix for the enrichments with  $\mathbf{N}_c$  denoting the vector with the  $C^{-1}$  enrichment functions [26] and  $\mathbf{R}$  the rotation matrix that transforms the quantities from the global coordinate systems to their counterparts in the enrichment coordinate systems.  $\Omega_e$ ,  $\partial\Omega_e^c$  and  $\partial\Omega_e^t$  respectively denote the (regular or interface-enriched) finite elements, the cohesive interfaces (with cohesive tractions  $\mathbf{t}_c$ ) and the edges along which tractions  $\mathbf{s}_t$  are applied;  $\mathbf{b}$  is the body force vector and  $\boldsymbol{\sigma}$  denote the stresses. The cohesive model adopted in this work is the exponential cohesive law introduced by Ortiz and Pandolfi [28] and described by the critical stress (or strength) of the interface,  $\sigma_c$ , the critical opening displacement,  $\delta_c$ , and the mode mixity parameter,  $\beta$ . An effective displacement jump  $\delta_e$  is defined by the normal opening  $\delta_n$  and shear opening  $\delta_s$  as

$$\delta_e = \sqrt{\delta_n^2 + \beta^2 \delta_s^2}, \quad (2)$$

in which,  $\beta$  denotes the mode mixity factor and is chosen to be 1. The cohesive law takes the form

$$\mathbf{t} = \frac{t}{\delta_e} [\beta^2 \boldsymbol{\delta} + (1 - \beta^2) \delta_n \mathbf{n}], \quad (3)$$

where  $\boldsymbol{\delta}$  is the displacement jump vector,  $\mathbf{n}$  is the unit vector normal to the cohesive interface, and the scalar effective traction,  $t$ , is given by

$$t = \begin{cases} \delta_e \frac{\sigma_c}{\delta_c} e^{1-\delta/\delta_c} & \text{loading} \\ \delta_e \frac{\sigma_c}{\delta_c} e^{1-\delta/\delta_{max}} & \text{unloading} \end{cases}, \quad (4)$$

in which,  $\delta_{max}$  is an internal state variable that stores the maximum effective opening, and  $\delta_c$  is the critical opening corresponding to the maximum traction. A linear unloading behavior toward origin is also adopted to model the unrecoverable failure upon interface closure. Under normal closure, the shear response is assumed to be the same as in opening, and to prevent interpenetration of interfaces, the normal traction follows [29]

$$t_n = e \frac{\sigma_c}{\alpha} \sinh\left(\frac{\alpha \delta_n}{\delta_c}\right), \text{ if } \delta_n < 0, \quad (5)$$

where  $e$  is the Euler's number and  $\alpha$  is a dimensionless parameter that controls the growth of compressive normal traction which is chosen to be 100 in the current study.

To allow for the simulations of realistic models of the composite laminate with hundreds of fibers, the cohesive IGFEM solver used in this study was implemented in parallel [30] using the PETSc library [31] and an adaptive load-stepping scheme [32]. To improve the convergence of the nonlinear cohesive IGFEM solver, an adaptive damping scheme [33] was also included.

## 2.2 Sensitivity to geometrical parameters of individual fibers

Figure 2 illustrates the type of problems investigated in this work. The virtual model of the  $[0/90/0]_T$  composite laminate is composed of two glass/epoxy  $0^\circ$  plies modeled as linearly elastic layers with homogenized properties described by the Halpin-Tsai relation [34] and a  $90^\circ$  carbon/epoxy ply with hundreds of fibers whose radii and locations are taken from optical images [22]. The matrix and fibers in the  $90^\circ$  are assumed to behave elastically. Figure 2 also illustrates the boundary conditions adopted in this work, with the transverse strain value  $\bar{\epsilon}$  imposed by applying a uniform transverse displacement along the right edge of the domain.

Under displacement-controlled loading and in the absence of body forces and tractions, the external force associated with free nodes on the right-hand side of Eq. (1) vanishes. The resulting system of equations at load increment  $n$  becomes

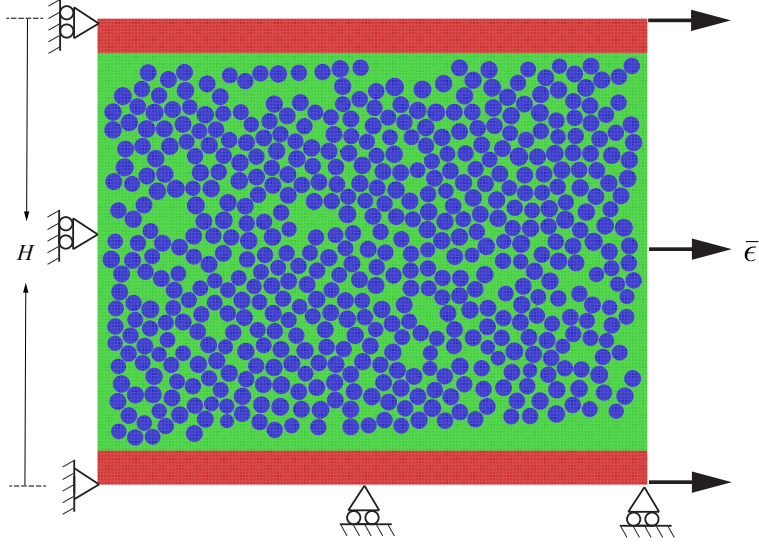


Figure 2: Schematic illustration of the  $[0, 90, 0]_T$  laminate subjected to strain-controlled loading.

$${}^n\mathbf{F}_{int}({}^n\mathbf{U}(\bar{\epsilon}, \mathbf{d}), \mathbf{d}) = \begin{bmatrix} {}^n\mathbf{F}_{int}^f \\ {}^n\mathbf{F}_{int}^p \end{bmatrix} = \begin{bmatrix} \mathbf{0} \\ {}^n\mathbf{F}_{ext} \end{bmatrix}, \quad (6)$$

where the superscript  $f$  and  $p$  respectively indicate free and prescribed nodes, the internal force vector  ${}^n\mathbf{F}_{int}$  corresponds to the left-hand side of Eq. (1) and has non-zero value only at the prescribed nodes.

The resulting average transverse stress at load increment  $n$  is given by

$${}^n\bar{\sigma} = \mathbf{L}^T {}^n\mathbf{F}_{int} / H, \quad (7)$$

in which  $H$  denotes the width of the specimen and  $\mathbf{L}^T$  is a constant row vector composed of 1 and 0 that extracts the right edge reactions from the internal force vector  ${}^n\mathbf{F}_{int}$ . For simplicity, the leading superscript  $n$  will be omitted in the remainder of the derivation.

Due to the dependency of the internal force on both  $\mathbf{U}$  and  $\mathbf{d}$ , the sensitivity of the transverse stress  $\bar{\sigma}$  with respect to the design variables takes the form

$$\frac{d\bar{\sigma}}{d\mathbf{d}} = \frac{\partial \bar{\sigma}}{\partial \mathbf{U}}^* \mathbf{U} + \frac{\partial \bar{\sigma}}{\partial \mathbf{d}}, \quad (8)$$

in which  $(\ )^*$  denotes the shape material derivative defined as

$$\mathbf{U}^*(\mathbf{x}, \mathbf{d}) = \frac{\partial \mathbf{U}}{\partial \mathbf{d}} + \nabla \mathbf{U} \cdot \mathbf{V}. \quad (9)$$

An interpretation of the shape material derivative is that it is essentially the derivative with

respect to the geometrical parameters and consider the dependency of nodal coordinates  $\mathbf{x}$  on the geometrical parameters  $\mathbf{d}$  due to enrichment. In (9),  $\mathbb{V} = \frac{d\mathbf{x}}{d\mathbf{d}}$  corresponds to the shape velocity field, which, due to the stationary nature of the non-conforming mesh, vanishes everywhere except at the enriched nodes, thereby greatly reducing the computational cost.

Calculating the terms  $\frac{\partial \bar{\sigma}}{\partial \mathbf{U}}$  and  $\frac{\partial \bar{\sigma}}{\partial \mathbf{d}}$  in (8) readily yields

$$\frac{\partial \bar{\sigma}}{\partial \mathbf{U}} = \frac{1}{H} \mathbf{L}^T \frac{\partial \mathbf{F}_{int}}{\partial \mathbf{U}} = \frac{1}{H} \mathbf{L}^T \mathbf{K}_T, \quad (10)$$

and

$$\frac{\partial \bar{\sigma}}{\partial \mathbf{d}} = \frac{1}{H} \mathbf{L}^T \frac{\partial \mathbf{F}_{int}}{\partial \mathbf{d}}, \quad (11)$$

where  $\mathbf{K}_T$  denotes the tangent stiffness matrix.

To complete the calculation of the sensitivities in (8), we compute  $\bar{\mathbf{U}}$  by taking the derivative of both sides of (1) with respect to  $\mathbf{d}$  as

$$\begin{aligned} \mathbf{A}_e \left\{ \int_{\Omega_e} \left[ \mathbf{B}^T \boldsymbol{\sigma}(\mathbf{U}, \mathbf{d}) + \mathbf{B}^T \left( \mathbb{C}(\mathbf{B}\mathbf{U} + \mathbf{B}\bar{\mathbf{U}}) + \sigma \operatorname{div}(\mathbb{V}) \right) \right] dA \right\} + \\ \mathbf{A}_e \left\{ \int_{\partial\Omega_e^c} \left[ \mathbf{B}_c^T \mathbf{t}_c + \mathbf{B}_c^T \left( \mathbb{A}(\mathbf{B}_c\mathbf{U} + \mathbf{B}_c\bar{\mathbf{U}}) + \mathbf{t}_c \operatorname{div}_\Gamma(\mathbb{V}) \right) \right] dS \right\} = \mathbf{0}, \quad (12) \end{aligned}$$

in which  $\mathbb{C}$  and  $\mathbb{A}$  are the consistent tangent moduli for the material constitutive laws of the regular 2D elements and of the cohesive elements, respectively. In the current analysis, the matrix and fibers are assumed to behave elastically, hence  $\mathbb{C}$  is the stiffness tensor. For the cohesive elements,  $\mathbb{A}$  is obtained by differentiating the traction-separation relation with respect to the separation. The symbols  $\operatorname{div}$  and  $\operatorname{div}_\Gamma$  respectively denote the divergence and contour divergence defined as

$$\operatorname{div}(\mathbb{V}_i) = \operatorname{tr} \left( \frac{\partial \mathbb{V}_i}{\partial \mathbf{x}} \right), \quad (13)$$

and

$$\operatorname{div}_\Gamma(\mathbb{V}_i) = \operatorname{tr} \left[ \left( \mathbf{I} - \mathbf{n}\mathbf{n}^T \right) \frac{\partial \mathbb{V}_i}{\partial \mathbf{x}} \right], \quad (14)$$

where  $\mathbf{n}$  is the outward unit normal vector of  $\Gamma$ . We note that the contour divergence is the 1D counterpart of surface divergence, obtained by considering the projection of shape velocity onto  $\Gamma$ .

To illustrate the derivation of the shape velocity  $\mathbb{V}$  for the problem at hand, let us consider an enrichment node  $\mathbf{x} = (x, y)$  at the intersection of  $i^{\text{th}}$  fiber defined by  $f(x_{ci}, y_{ci}, R_i) = 0$  and an element edge defined by  $g(x, y) = 0$  (Fig. 3). The coordinates of the intersection satisfy

$$\begin{cases} g(x, y) = (y_1 - y_2)x + (x_2 - x_1)y + y_1(x_1 - x_2) - x_1(y_1 - y_2) = 0, \\ f(x, y) = (x - x_{ci})^2 + (y - y_{ci})^2 - R_i^2 = 0. \end{cases} \quad (15)$$

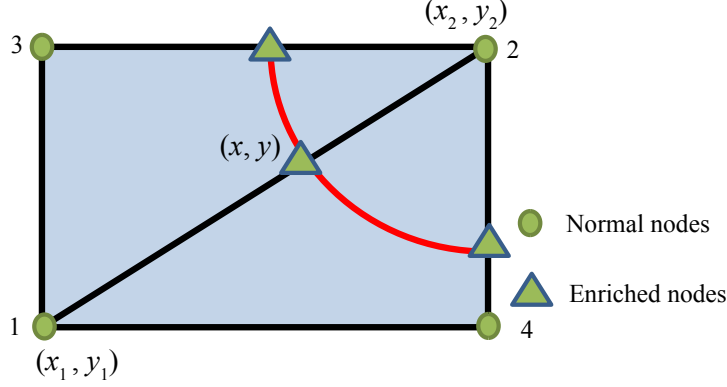


Figure 3: Schematic illustration of the enrichment nodes: two triangular elements (1-2-3 and 1-4-2) intersected by the  $i^{th}$  fiber, introducing enriched nodes on the element edges.

Differentiating (15) with respect to the fiber radius  $R_i$  yields

$$\begin{bmatrix} y_1 - y_2 & x_2 - x_1 \\ 2x - 2x_{ci} & 2y - 2y_{ci} \end{bmatrix} \begin{Bmatrix} \frac{dx}{dR_i} \\ \frac{dy}{dR_i} \end{Bmatrix} = \begin{Bmatrix} 0 \\ 2R_i \end{Bmatrix}, \quad (16)$$

from which  $\frac{d\mathbf{x}}{dR_i}$  can readily be obtained. Similarly,  $\frac{d\mathbf{x}}{dx_{ci}}$  and  $\frac{d\mathbf{x}}{dy_{ci}}$  can be obtained by differentiating (15) with respect to  $x_{ci}$  and  $y_{ci}$ . These derivatives constitute the shape velocity field, and reflect how the nodal coordinates move with respect to the shape parameters. It immediately becomes clear that the shape velocity field is only non-zero at enriched nodes. The calculated shape velocity can then be used to extract the divergence and contour divergence in Eqs. (13) and (14).

Rearranging Eq. (12), we obtain

$$\begin{aligned} \mathbf{A}_e \left\{ \int_{\Omega_e} \mathbf{B}^T \mathbf{C} \mathbf{B}^* \mathbf{U} dA + \int_{\partial\Omega_e^c} \mathbf{B}_c^T \mathbf{A} \mathbf{B}_c^* \mathbf{U} dS \right\} = - \mathbf{A}_e \left\{ \int_{\Omega_e} \left[ \mathbf{B}^T \boldsymbol{\sigma} + \mathbf{B}^T \mathbf{C} \mathbf{B}^* \mathbf{U} + \mathbf{B}^T \boldsymbol{\sigma} \operatorname{div}(\mathbb{V}) \right] dA \right\} \\ - \mathbf{A}_e \left\{ \int_{\partial\Omega_e^c} \left[ \mathbf{B}_c^T \mathbf{t}_c(\mathbf{U}, \mathbf{d}) + \mathbf{B}_c^T \mathbf{A} \mathbf{B}_c^* \mathbf{U} + \mathbf{B}_c^T \mathbf{t}_c \operatorname{div}_\Gamma(\mathbb{V}) \right] dS \right\}, \quad (17) \end{aligned}$$

which can be rewritten as

$$\mathbf{K}_T^* \mathbf{U} = -\mathbf{F}_{ps} \quad (18)$$

It should be noted that the  $\mathbf{K}_T$  matrix appearing in the so-called pseudo-analysis (Eq. (18)) is the same as that evaluating the primary problem (Eq. (1)). One thus only needs to compute the pseudo load vector  $\mathbf{F}_{ps}$  and take advantage of the already factorized  $\mathbf{K}_T$  matrix to compute  $\mathbf{U}^*$  and, from there, the sensitivities of  $\bar{\sigma}$  with respect to the shape parameters using Eq. (8). The derivation of the terms  $\mathbf{B}^*$  and  $\mathbf{B}_c^*$  appearing in Eq. (17) can be found in Ref. [10] and are presented for completeness for the case of the cohesive IGFEM in Appendix A.

## 2.3 Sensitivity to distributions of geometrical parameters

We now turn our attention to the sensitivity of the transverse response of the composite laminate to the parameters that define the *distribution* of the microstructural geometrical parameters. For example, building on the sensitivities of the transverse stress-strain curve with respect to the radius of each fiber derived in the previous section, we now aim to obtain the sensitivity of the transverse response with respect to the mean ( $\mu_R$ ) and standard deviation ( $s_R$ ) of the distribution of fiber radii present in the 90° ply. We note that the IGFEM-based shape sensitivity analysis method can be applied to a wide range of geometrical parameters and their distribution parameters that characterize the microstructure. The sensitivities with respect to the distribution parameters are quite complex as to be seen, and depend on not only the sensitivities with respect to individual fiber radius and location, but also how the fiber radii and locations are changing. In the current study, we start our consideration for the sensitivity of the stress-strain response with respect to the mean and standard deviation of the fiber radii while keeping the fiber fixed.

Let us consider a general function of the design variables,  $f = f(\mathbf{d})$ , and derive the sensitivity of the transverse stress  $\bar{\sigma}$  with respect to  $f$ . Since  $f$  is a function of all individual variables, we need to specify the direction  $\mathbf{v}$  along which the change of independent variables causes the change in  $f$ . Accordingly, the sensitivity along  $\mathbf{v}$  is calculated as

$$\left. \frac{\partial \bar{\sigma}}{\partial f} \right|_{\mathbf{v}} = \lim_{\zeta \rightarrow 0} \frac{\bar{\sigma}(\mathbf{d} + \zeta \mathbf{v}) - \bar{\sigma}(\mathbf{d})}{f(\mathbf{d} + \zeta \mathbf{v}) - f(\mathbf{d})} = \lim_{\zeta \rightarrow 0} \frac{\zeta \nabla_{\mathbf{d}} \bar{\sigma} \cdot \mathbf{v}}{\zeta \nabla_{\mathbf{d}} f \cdot \mathbf{v}} = \frac{\nabla_{\mathbf{d}} \bar{\sigma} \cdot \mathbf{v}}{\nabla_{\mathbf{d}} f \cdot \mathbf{v}}, \quad (19)$$

where  $\nabla_{\mathbf{d}} f$  is a row vector that contains the derivative of  $f$  with respect to the individual parameter (i.e.,  $\nabla_{\mathbf{d}} f = [\frac{\partial f}{\partial d_1}, \frac{\partial f}{\partial d_2}, \dots]$ ), and  $\nabla_{\mathbf{d}} \bar{\sigma}$  is a row vector that contains the sensitivities of the stress  $\bar{\sigma}$  with respect to individual design variable (i.e.,  $\nabla_{\mathbf{d}} \bar{\sigma} = [\frac{\partial \bar{\sigma}}{\partial d_1}, \frac{\partial \bar{\sigma}}{\partial d_2}, \dots]$ ).

If the vector  $\mathbf{d}$  of design variables only contains the radii of the  $n$  fibers, i.e.,  $\mathbf{d} = \mathbf{R} = (R_1, R_2, \dots, R_n)$ , and if  $f$  denotes the mean or standard deviation of the fiber radius distribution, substituting the expression of the mean and standard deviation into Eq. (19) readily yields the sensitivity of the transverse stress with respect to the mean and standard deviation of fiber radii by changing the radii  $\mathbf{R}$  along the direction  $\mathbf{v}$ .

However, among all possible choices of the direction vector  $\mathbf{v}$ , we need to find out meaningful directions along which the sensitivities are calculated. One choice is to calculate the sensitivity with respect to mean fiber radii while keeping the standard deviation constant, and to calculate the sensitivity with respect to the standard deviation of the fiber radii while keeping the mean constant. As illustrated graphically in Ref. [27], this can be achieved by choosing the directions  $\mathbf{v}_1 = [1, 1, \dots, 1]/\sqrt{n}$  and  $\mathbf{v}_2 = [R_1 - \mu_R, R_2 - \mu_R, \dots, R_n - \mu_R]/\sqrt{\sum_{i=1}^n (R_i - \mu_R)^2}$  to compute the sensitivities with respect to the mean and standard deviation of the fiber radius distribution, respectively. We further demonstrate in Appendix B that the direction  $\mathbf{v}_1 = [1, 1, \dots, 1]/\sqrt{n}$  used to compute the sensitivity with respect to the mean (first-order moment) fiber radius keeps the other moments of  $\mathbf{R}$  up to  $n^{\text{th}}$  order unchanged. Similarly, calculating the sensitivity

with respect to the standard deviation (second-order moment) of  $\mathbf{R}$  along the direction of  $\mathbf{v}_2 = [R_1 - \mu_R, R_2 - \mu_R, \dots, R_n - \mu_R] / \sqrt{\sum_{i=1}^n (R_i - \mu_R)^2}$  not only keeps the mean value constant, but also keeps all moments of  $\mathbf{R}$  of order  $i = 3, \dots, n$  unchanged. Substituting the expression of  $\mathbf{v}_1$  and  $\mathbf{v}_2$  into Eq. (19), we obtain the expression of the sensitivities of  $\bar{\sigma}$  with respect to the mean and standard deviation of  $\mathbf{R}$  along  $\mathbf{v}_1$  and  $\mathbf{v}_2$  as

$$\left. \frac{\partial \bar{\sigma}}{\partial \mu_R} \right|_{\mathbf{v}_1} = \nabla_{\mathbf{R}} \bar{\sigma} \cdot [1, 1, \dots, 1]^T, \quad (20)$$

and

$$\left. \frac{\partial \bar{\sigma}}{\partial s_R} \right|_{\mathbf{v}_2} = \nabla_{\mathbf{R}} \bar{\sigma} \cdot [R_1 - \mu_R, R_2 - \mu_R, \dots, R_n - \mu_R]^T / s_R, \quad (21)$$

where  $\nabla_{\mathbf{R}} \bar{\sigma}$  is a row vector that contains the sensitivities of stress with respect to individual fiber radius calculated in Section. 2.2 (i.e.,  $\nabla_{\mathbf{R}} \bar{\sigma} = [\frac{\partial \bar{\sigma}}{\partial R_1}, \frac{\partial \bar{\sigma}}{\partial R_2}, \dots, \frac{\partial \bar{\sigma}}{\partial R_n}]$ ).

## 2.4 Sensitivity with respect to nearest-neighbor distance

The nearest-neighbor distance is an important quantity related to the initiation and propagation of interface debonding, as it directly determines the amplitude of the stress concentration present along the interfaces of two adjacent fibers. For fiber  $i$  (with radius  $R_i$ ) with fiber  $j$  (with radius  $R_j$ ) as its closest neighbor, the nearest-neighbor distance is given by

$$\delta_{ij} = [(x_{ci} - x_{cj})^2 + (y_{ci} - y_{cj})^2]^{1/2} - R_i - R_j. \quad (22)$$

Due to the dependency of  $\delta_{ij}$  on the center coordinates and radii of fiber  $i$  and  $j$ , i.e.,  $\mathbf{d} = (x_{ci}, y_{ci}, R_i, x_{cj}, y_{cj}, R_j)$ , we can calculate the sensitivity of stress with respect to  $\delta_{ij}$  along any direction  $\mathbf{v} = [\Delta x_{ci}, \Delta y_{ci}, \Delta R_i, \Delta x_{cj}, \Delta y_{cj}, \Delta R_j]$  while the positions and radii of all other fibers are fixed. Following Eq. (19), the sensitivity of  $\bar{\sigma}$  with respect to  $\delta_{ij}$  is thus given by

$$\left. \frac{\partial \bar{\sigma}}{\partial \delta_{ij}} \right|_{\mathbf{v}} = \frac{\frac{\partial \bar{\sigma}}{\partial x_{ci}} \Delta x_{ci} + \frac{\partial \bar{\sigma}}{\partial y_{ci}} \Delta y_{ci} + \frac{\partial \bar{\sigma}}{\partial R_i} \Delta R_i + \frac{\partial \bar{\sigma}}{\partial x_{cj}} \Delta x_{cj} + \frac{\partial \bar{\sigma}}{\partial y_{cj}} \Delta y_{cj} + \frac{\partial \bar{\sigma}}{\partial R_j} \Delta R_j}{[(x_{ci} - x_{cj})(\Delta x_{ci} - \Delta x_{cj}) + (y_{ci} - y_{cj})(\Delta y_{ci} - \Delta y_{cj})] / (\delta_{ij} + R_i + R_j) - \Delta R_i - \Delta R_j}. \quad (23)$$

We can also calculate the sensitivity of  $\bar{\sigma}$  with respect to the mean and standard deviation of nearest-neighbor distances,  $\mu_\delta$  and  $s_\delta$ . For a microstructure composed of  $n$  fibers, the nearest-neighbor information can be described by a  $n \times 2$  fiber pair matrix  $\mathbf{P}$ , with the first column of  $\mathbf{P}$  containing the fiber ID from 1 to  $n$  and the second column the fiber ID of the corresponding closest fiber. For example, Fig. 4 illustrates a three-fiber microstructure for which the fiber pair matrix is  $\mathbf{P} = [1, 2; 2, 1; 3, 2]$ .

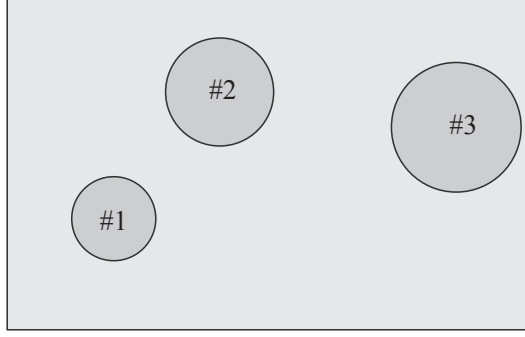


Figure 4: Illustration of a three-fiber microstructure with  $\mathbf{P} = [1, 2; 2, 1; 3, 2]$ .

The mean and standard deviation of the nearest-neighbor distances are expressed as

$$\mu_\delta = \frac{1}{n} \sum_{j=1}^n \delta_{P(j,1)P(j,2)}, \quad (24)$$

and

$$s_\delta = \sqrt{\frac{1}{n-1} \sum_{j=1}^n (\delta_{P(j,1)P(j,2)} - \mu_\delta)^2}. \quad (25)$$

When all fiber center coordinates and radii are considered as design variables, the sensitivity of the transverse stress with respect to  $\mu_\delta$  along any direction  $\mathbf{v} = [\Delta x_{c1}, \Delta y_{c1}, \Delta R_1, \Delta x_{c2}, \Delta y_{c2}, \Delta R_2, \dots, \Delta x_{cn}, \Delta y_{cn}, \Delta R_n]$  is derived from Eq. (19) as

$$\left. \frac{\partial \bar{\sigma}}{\partial \mu_\delta} \right|_{\mathbf{v}} = \sum_{i=1}^n \left( \frac{\partial \bar{\sigma}}{\partial x_{ci}} \Delta x_{ci} + \frac{\partial \bar{\sigma}}{\partial y_{ci}} \Delta y_{ci} + \frac{\partial \bar{\sigma}}{\partial R_i} \Delta R_i \right) \Bigg/ \sum_{i=1}^n \left( \frac{\partial \mu_\delta}{\partial x_{ci}} \Delta x_{ci} + \frac{\partial \mu_\delta}{\partial y_{ci}} \Delta y_{ci} + \frac{\partial \mu_\delta}{\partial R_i} \Delta R_i \right), \quad (26)$$

in which

$$\frac{\partial \mu_\delta}{\partial x_{ci}} = \frac{1}{n} \sum_{j=1}^n \frac{\partial \delta_{P(j,1)P(j,2)}}{\partial x_{ci}} = \frac{1}{n} \sum_{j=1}^n \left[ \delta^k(i, P(j,1)) \frac{\partial \delta_{iP(j,2)}}{\partial x_{ci}} + \delta^k(i, P(j,2)) \frac{\partial \delta_{P(j,1)i}}{\partial x_{ci}} \right], \quad (27)$$

where  $\delta^k$  denotes the Kronecker delta, i.e.,  $\delta^k(i, j) = 1$  if  $i = j$ ; 0 if  $i \neq j$ . The derivatives  $\frac{\partial \mu_\delta}{\partial y_{ci}}$  and  $\frac{\partial \mu_\delta}{\partial R_i}$  can be calculated similarly. The sensitivity of stress with respect to  $s_\delta$  along  $\mathbf{v}$  is calculated as

$$\left. \frac{\partial \bar{\sigma}}{\partial s_\delta} \right|_{\mathbf{v}} = \sum_{i=1}^n \left( \frac{\partial \bar{\sigma}}{\partial x_{ci}} \Delta x_{ci} + \frac{\partial \bar{\sigma}}{\partial y_{ci}} \Delta y_{ci} + \frac{\partial \bar{\sigma}}{\partial R_i} \Delta R_i \right) \Bigg/ \sum_{i=1}^n \sum_{j=1}^n \left\{ \left( \delta_{P(j,1)P(j,2)} - \mu_\delta \right) \left[ \left( \frac{\partial \delta_{P(j,1)P(j,2)}}{\partial x_{ci}} - \frac{\partial \mu_\delta}{\partial x_{ci}} \right) \Delta x_{ci} + \left( \frac{\partial \delta_{P(j,1)P(j,2)}}{\partial y_{ci}} - \frac{\partial \mu_\delta}{\partial y_{ci}} \right) \Delta y_{ci} + \left( \frac{\partial \delta_{P(j,1)P(j,2)}}{\partial R_i} - \frac{\partial \mu_\delta}{\partial R_i} \right) \Delta R_i \right] \right\}, \quad (28)$$

where the calculation of the derivatives of  $\delta_{P(j,1)P(j,2)}$  with respect to  $x_{ci}$ ,  $y_{ci}$  and  $R_i$  follows Eq. (27).

If we only consider the effect of the fiber radii and keep all fiber locations fixed, i.e.,  $\mathbf{v} = [\Delta_{R_1}, \Delta_{R_2}, \dots, \Delta_{R_n}]$ , Eqs. (26) and (28) reduce to

$$\left. \frac{\partial \bar{\sigma}}{\partial \mu_\delta} \right|_{\mathbf{v}} = n \sum_{i=1}^n \frac{\partial \bar{\sigma}}{\partial R_i} \Delta R_i \Big/ \sum_{i=1}^n \sum_{j=1}^n \left[ -\delta^k(i, P(j, 1)) - \delta^k(i, P(j, 2)) \right] \Delta R_i, \quad (29)$$

and

$$\left. \frac{\partial \bar{\sigma}}{\partial s_\delta} \right|_{\mathbf{v}} = (n-1)s_\delta \sum_{i=1}^n \frac{\partial \bar{\sigma}}{\partial R_i} \Delta R_i \Big/ \sum_{i=1}^n \sum_{j=1}^n \left\{ \left( \delta_{P(j,1)P(j,2)} - \mu_\delta \right) \left[ -\delta^k(i, P(j, 1)) - \delta^k(i, P(j, 2)) \right] + \sum_{k=1}^n \left( \delta^k(i, P(k, 1)) + \delta^k(i, P(k, 2)) \right) \right\} \Delta R_i. \quad (30)$$

While the direction  $\mathbf{v}$  along which the sensitivities are calculated is arbitrary, we again adopt the directions  $\mathbf{v}_1 = [1, 1, \dots, 1]/\sqrt{n}$  and  $\mathbf{v}_2 = [R_1 - \mu_R, R_2 - \mu_R, \dots, R_n - \mu_R]/\sqrt{\sum_{i=1}^n (R_i - \mu_R)^2}$  when calculating the sensitivities with respect to the mean and standard deviation of the nearest-neighbor distance distribution, respectively. This choice leads to

$$\left. \frac{\partial \bar{\sigma}}{\partial \mu_\delta} \right|_{\mathbf{v}_1} = -\frac{1}{2} \nabla_{\mathbf{R}} \bar{\sigma} \cdot [1, 1, \dots, 1]^T \quad (31)$$

and

$$\left. \frac{\partial \bar{\sigma}}{\partial s_\delta} \right|_{\mathbf{v}_1} = (n-1)s_\delta \sum_{i=1}^n \frac{\partial \bar{\sigma}}{\partial R_i} (R_i - \mu_R) \Big/ \sum_{i=1}^n \sum_{j=1}^n \left\{ \left( \delta_{P(j,1)P(j,2)} - \mu_\delta \right) \left[ -\delta^k(i, P(j, 1)) - \delta^k(i, P(j, 2)) \right] + \sum_{k=1}^n \left( \delta^k(i, P(k, 1)) + \delta^k(i, P(k, 2)) \right) \right\} (R_i - \mu_R). \quad (32)$$

By comparing Eqs. (31) and (20), we note that the sensitivity of  $\bar{\sigma}$  with respect to the mean of the nearest-neighbor distance is  $-0.5$  times of the sensitivity of  $\bar{\sigma}$  with respect to the mean fiber radius, when the change of fiber radii follow the direction of  $\mathbf{v}_1$ . This result is due to the fact that, if all fiber radii increase by the same amount  $\delta R$ , the nearest-neighbor distance between all fiber pairs decreases by  $2\delta R$ , leading to a decrease of  $2\delta R$  in the mean nearest-neighbor distance.

### 3 Numerical Verification

In order to verify the expression of the sensitivities of the transverse response with respect to individual shape parameters and to the corresponding distribution parameters, we compare

in this section the analytical values derived previously to finite difference approximations for the case of the simple two-fiber microstructure shown in Fig. 5 (a). In this verification problem, the radii of the first (red) and second (green) fiber are chosen to be 4 and 3  $\mu\text{m}$ , respectively. The strength values of the two fiber-matrix interfaces are respectively set to be 40 and 30 MPa, and both interfaces are assumed to have the same critical opening  $\delta_c = 50 \mu\text{m}$ . The elastic moduli of the fiber and matrix are 19.5 and 2.38 GPa, with Poisson's ratios of 0.45 and 0.43, respectively [26].

Figure 5 (b) presents the sensitivity of the transverse stress  $\bar{\sigma}$  with respect to the radii of the two fibers. For the finite difference approximations, separate simulations were conducted by perturbing the fiber radii by a small magnitude  $\pm\delta_R=0.0001 \mu\text{m}$  and using the central difference approximation of the sensitivities. As apparent in the figure, very good agreement is observed between direct calculations and finite difference approximations of the sensitivities  $\partial\bar{\sigma}/\partial R_1$  and  $\partial\bar{\sigma}/\partial R_2$ . As expected, these two sensitivities are initially positive since larger fibers which are stiffer than the surrounding matrix would lead to a stiffer transverse stress-strain response. The larger fiber (Fiber 1) has a higher sensitivity since the same increase in fiber radius in the larger fiber results in a larger increase in fiber volume fraction. Once interfacial failure starts, the sensitivities become negative since cohesive failure is promoted in larger fibers, thereby affecting negatively the stress-strain curve. Once the interface of the larger fiber (Fiber 1) fails (at a strain level of about 0.02),  $\partial\bar{\sigma}/\partial R_1$  drops sharply while  $\partial\bar{\sigma}/\partial R_2$  temporarily becomes positive again before dropping sharply again once the interface of the second fiber fails. The temporary switching of the sign of  $\partial\bar{\sigma}/\partial R_2$  can be explained by the temporary unloading of the second interface during the cohesive failure of the interface of the first fiber. The unloading/reloading of the interfaces is illustrated in Fig. 6, which presents the evolution of percentage of failing ( $\delta_e \geq \delta_c$ ) and fully failed ( $\delta_e \geq 3\delta_c$ ) cohesive elements.

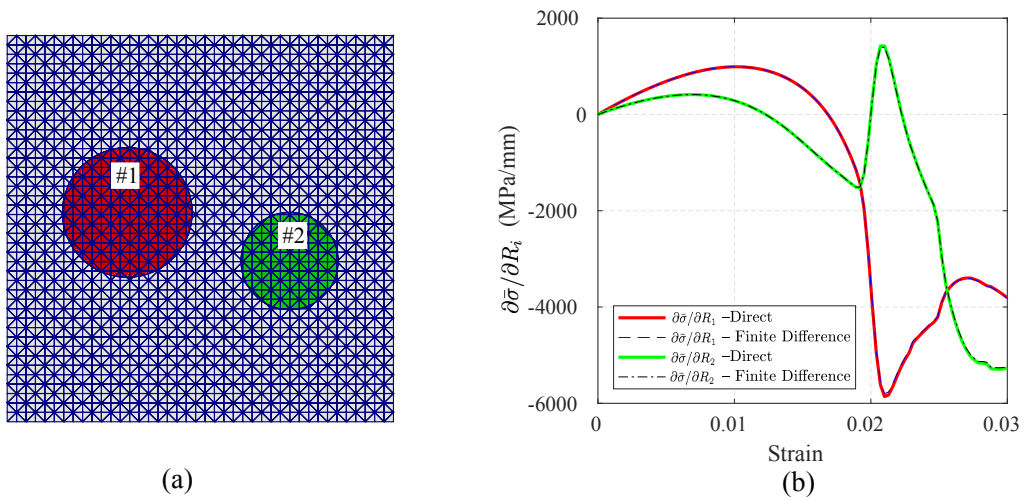


Figure 5: Verification of the sensitivity calculation: (a) IGFEM discretization of a two-fiber microstructure; (b) Comparison between direct calculations and finite difference approximations of the sensitivities of  $\bar{\sigma}$  with respect to the fiber radii  $R_1$  and  $R_2$ .

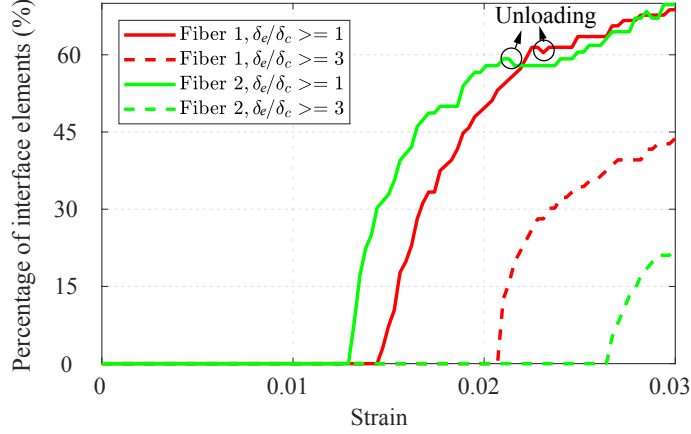


Figure 6: Temporary unloading of the fiber/matrix interfaces associated with the cohesive failure of the adjacent fiber: Evolution of percentage of failing ( $\delta_e \geq \delta_c$ ) and fully failed ( $\delta_e \geq 3\delta_c$ ) cohesive elements.

A similar agreement between direct calculations and finite difference approximations is obtained for the sensitivities of  $\bar{\sigma}$  with respect to the mean  $\mu_R$  and standard deviation  $s_R$  of the fiber radii, as shown in Fig. 7. As described in the previous section, the direct calculations are obtained by computing directional derivatives along the directions  $\mathbf{v}_1 = [1, 1]/\sqrt{2}$  and  $\mathbf{v}_2 = [1, -1]/\sqrt{2}$ , respectively, while the finite difference approximations are obtained by perturbing the fiber radii by  $\pm\delta_R\mathbf{v}_1$  and  $\pm\delta_R\mathbf{v}_2$ , respectively.

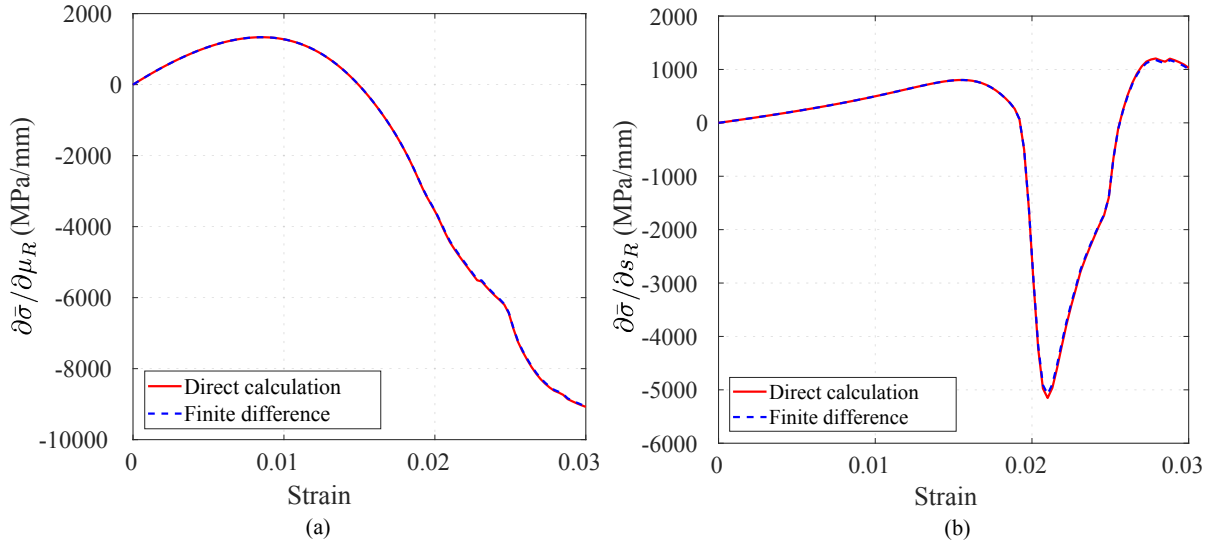


Figure 7: Verification of the sensitivity calculation with respect to: (a) mean fiber radii along the direction of  $\mathbf{v}_1 = (1, 1)/\sqrt{2}$ ; (b) standard deviation of fiber radii along the direction of  $\mathbf{v}_2 = (1, -1)/\sqrt{2}$ .

As apparent in Fig. 7(b), the sensitivity of  $\bar{\sigma}$  with respect to  $s_R$  is first positive before switching sign once the failure process starts. To confirm this result, we simulate the failure

response of a two-fiber microstructure with the same domain size, fiber placement, interfacial properties and mean fiber radius, but a slightly smaller standard deviation  $s_R$ :  $R_1 = 3.98 \mu\text{m}$  and  $R_2 = 3.02 \mu\text{m}$  (Fig. 8(a)). The corresponding transverse stress-strain curve is presented in Fig. 8(b), showing a small deviation from the response of the reference case  $R_1 = 4 \mu\text{m}$  and  $R_2 = 3 \mu\text{m}$  shown in Figure 5(a). Details of the transverse stress-strain curve are presented in Fig. 8(c,d), showing an increase in  $\bar{\sigma}$  prior to the interface failure (Fig. 8(c)) and a decrease in  $\bar{\sigma}$  during the failure event (Fig. 8(d)), as was suggested by the evolution of the sensitivity  $\partial\bar{\sigma}/\partial s_R$  shown in Fig. 7(b).

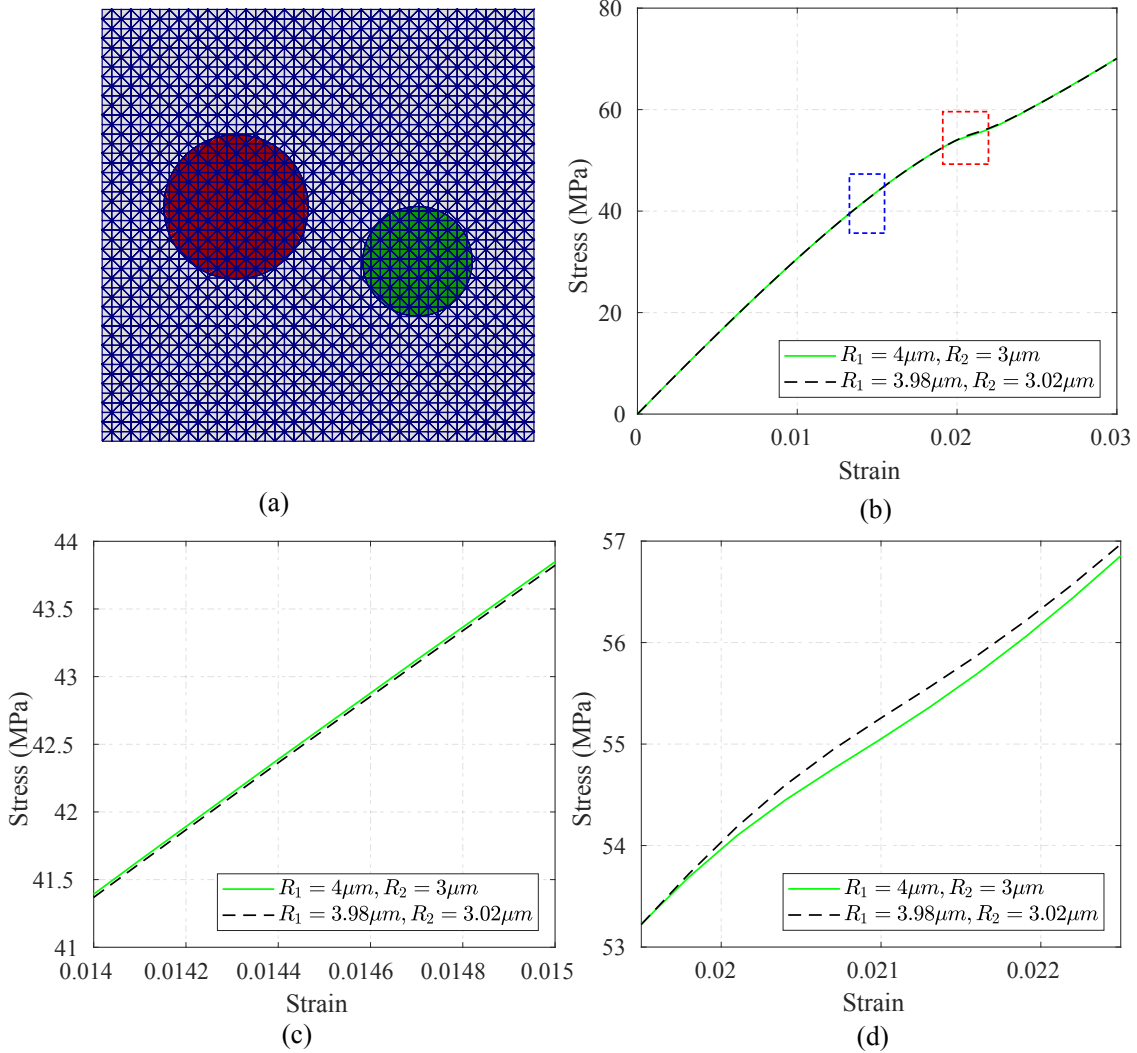


Figure 8: Verification of the sensitivity with respect to the standard deviation  $s_R$ : (a) IGFEM mesh of the microstructure with smaller standard deviation; (b) Stress-strain response comparison; (c)-(d) magnification of the regions highlighted by the blue and red boxes in (b).

## 4 Sensitivity Analysis on Realistic Microstructure

We now turn our attention to the sensitivity analysis of the transverse failure of the realistic microstructure shown earlier in Fig. 2. The width and thickness of the  $90^\circ$  ply are 0.228 and 0.165 mm, respectively, with two 0.014 mm thick  $0^\circ$  glass fiber plies placed on the top and bottom of the  $90^\circ$  ply. The  $90^\circ$  ply, reconstructed from experimental measurements using the image-based microstructure reconstruction tool set developed in Ref. [26], contains 531 carbon fibers and has a fiber volume fraction of 54%. The fiber radius distribution is described by a normal distribution with mean value  $\mu_R = 3.5 \mu\text{m}$  and standard deviation  $s_R = 0.143 \mu\text{m}$  (Fig. 9(a)), while the distribution of nearest-neighbor distances is described by a Weibull distribution (Fig. 9(b)). All interfaces have the same critical opening  $\delta_c = 75 \text{ nm}$  while 531 different cohesive strength ( $\sigma_c$ ) values are generated from a normal distribution with mean value of 24.06 MPa and standard deviation of 1.95 MPa and assigned to individual fiber/matrix interface. The choice of interface properties is within the ranges of experimental validated values in Refs. [25, 26]. The elastic properties for the homogenized  $0^\circ$  ply and for the matrix fibers in the  $90^\circ$  ply are taken from [26] and the properties of the matrix and fibers are the same as those in Section 3.

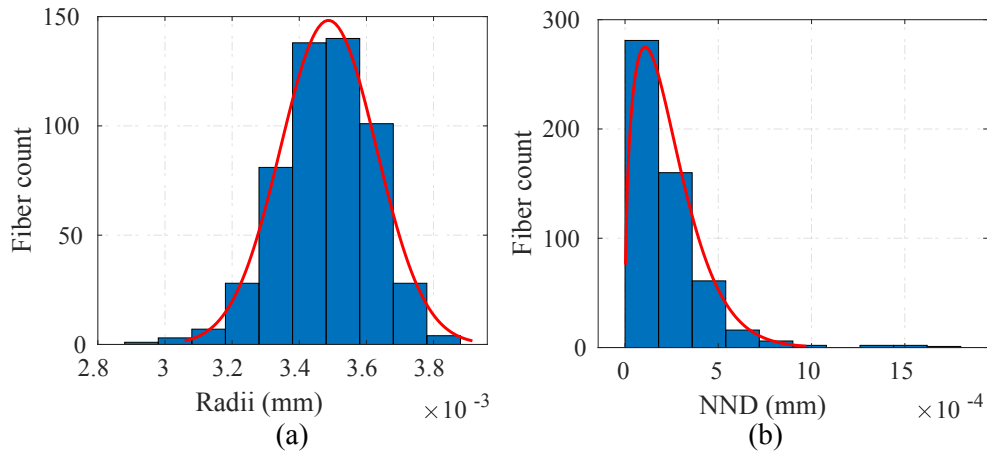


Figure 9: (a) Distribution of fiber radii fitted with a normal distribution; (b) Distribution of nearest-neighbor distance fitted with a Weibull distribution.

The microstructure is discretized with 254,646 3-node elements and 213,856 nodes, among which 85,816 nodes are enriched nodes. At places where the non-conforming triangular elements are intersected by the fiber/matrix interfaces, cohesive elements are considered, which introduces 213,856 cohesive elements along all fiber-matrix interfaces. When a 2% strain is applied along the  $0^\circ$  fibers direction, the simulation is completed using 254 time steps in 14.29 hours on 6 CPUs, out of which 10.63 hours are used for evaluating the sensitivities with respect to the 531 fiber radii. Hence the sensitivity analysis with respect to a single geometrical parameter is about 0.55% of the nonlinear IGFEM simulation, suggesting the high efficiency of sensitivity analysis with IGFEM.

The application of a 2% strain in the direction of the 0° fibers (Fig. 2) yields the nonlinear transverse stress-strain response shown in Fig. 10(a), which also presents the evolution of failing ( $\delta_e > \delta_c$ ) and failed ( $\delta_e > 3\delta_c$ ) cohesive elements. Four distinct stress drops corresponding to four sharp increases in the number of fully failed cohesive elements are observed in the stress-strain curve. As indicated in Fig. 10(b), these four stress drops are associated with the formation of transverse cracks in the 90° ply. These cracks and associated stress drops are labeled with numbers from 1 to 4. Experimental observations obtained by Montgomery [22] (also see Fig. 1 ) have shown that, under transverse loading, transverse cracks first appear in the 90-degree ply, and post-mortem analysis of the fracture surfaces indicated that about 95% of the failure event takes place along the fiber-matrix interfaces. This is the phenomenon of interest in this work, in which the matrix is considered to be linear elastic and the only damage model considered is the fiber-matrix interface failure. As shown in Fig. 10 (b), the simulated transverse cracks essentially consist in a series of fiber/matrix interface debonding connected by small matrix ligaments. The effect of these unbroken ligaments is relatively small and the displacement field in Fig. 10(c) shows the expected discontinuity across the transverse cracks.

We also observe that, while the percentage of fully failed element is monotonically increasing, the portion of cohesive elements reaching an effective displacement jump of  $\delta_c$  experiences a small drop at the formation of crack paths 2 and 4. This is indicative of the unloading of some elements located along adjacent cohesive interfaces.

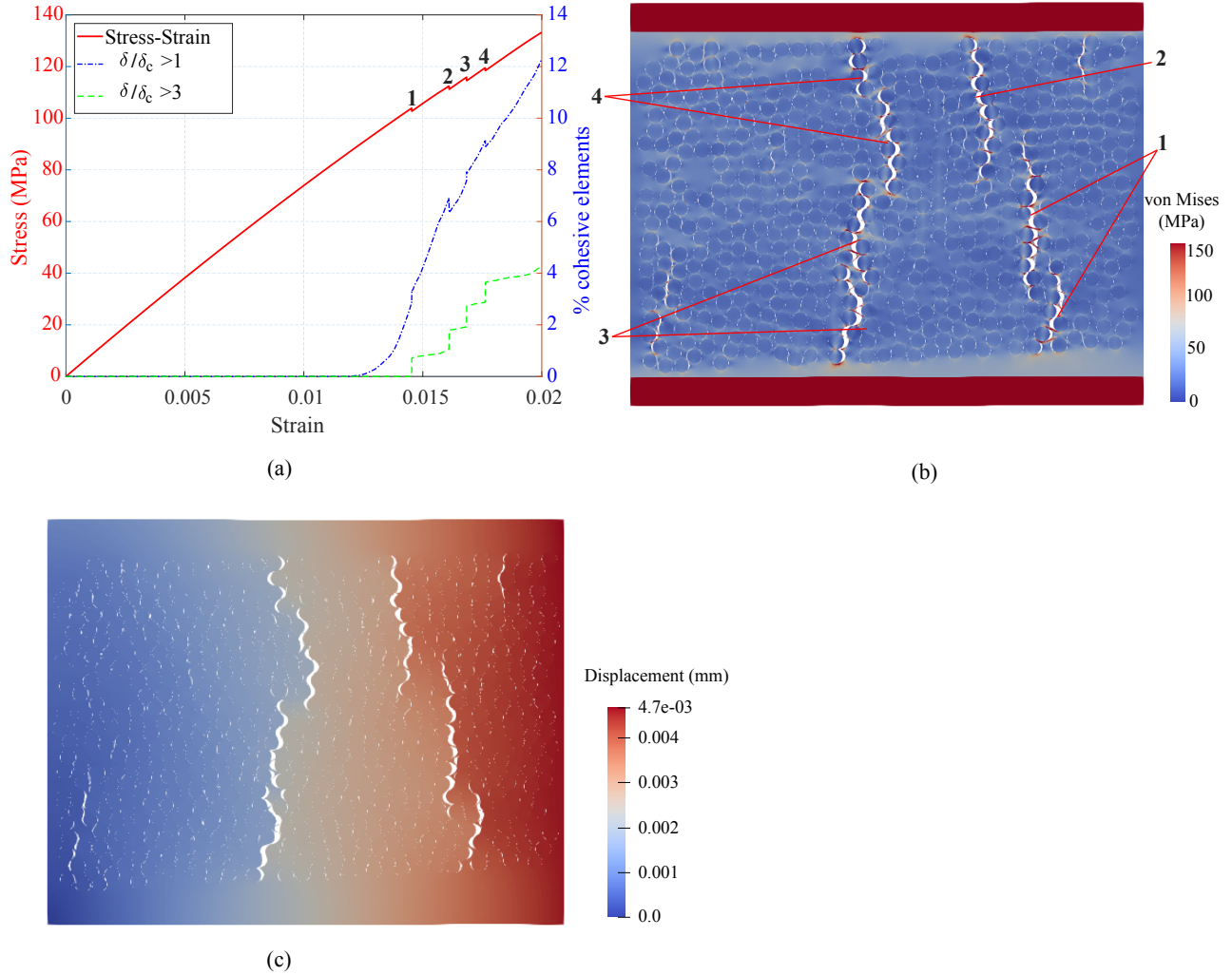


Figure 10: (a) Transverse stress-strain response and evolution of the portion of failing ( $\delta_e > \delta_c$ ) and failed ( $\delta_e > 3\delta_c$ ) cohesive elements; (b)-(c) von Mises stress and the X component of the displacement distribution on the deformed microstructure under 2% applied transverse strain, with the displacements amplified by a factor of 3 for visualization purpose. The cracks are labeled according to the stress drops they generated.

The evolution of the sensitivities of the transverse stress-strain curve with respect to every fiber radius  $\partial\bar{\sigma}/\partial R_i$  is shown in Figure 11(a). Each spike corresponds to the formation of a transverse crack in Fig. 10(b). The first portion of the sensitivity curves is magnified in Fig. 11(b), showing positive initial values as expected. Fig. 11(c) presents the spikes in sensitivities associated with the appearance of the first transverse crack. As apparent there, some of these first peak values are positive, others are negative.

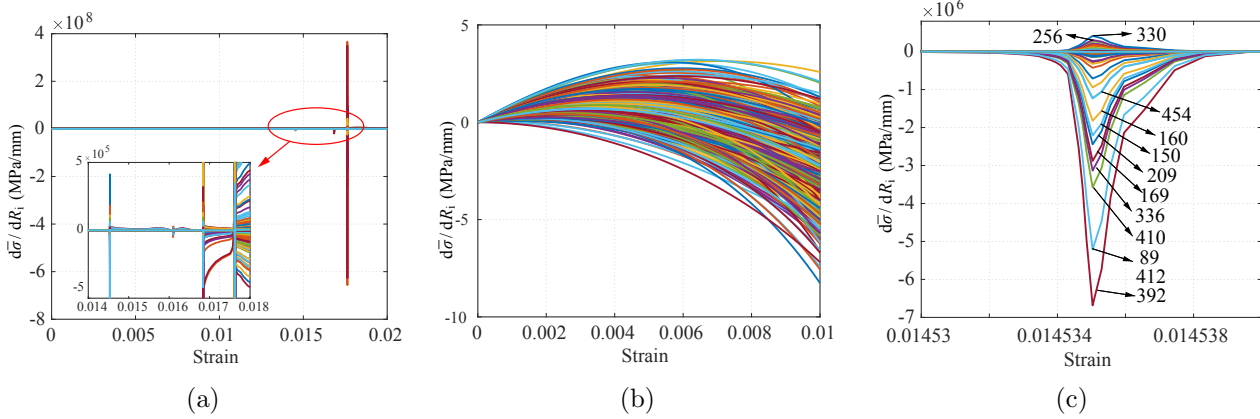


Figure 11: Evolution of the sensitivity of the transverse stress-strain curve with respect to individual fiber radii for the failure event described in Fig. 10(b). (a) Entire loading history; (b) Initial portion of the sensitivity curves; (c) Details of the sensitivity spikes associated with the first transverse crack.

To understand the physical significance of these shape sensitivities, we label in Fig. 11(c) the curves with the highest and lowest peak values with the ID number of the associated fibers and mark in Fig. 12 the ten fibers with the largest (positive) and smallest (negative) sensitivities in orange and blue, respectively. As apparent there, the fibers with the most negative sensitivities are located along the crack, while those with the most positive sensitivities are located in the vicinity of the transverse crack.

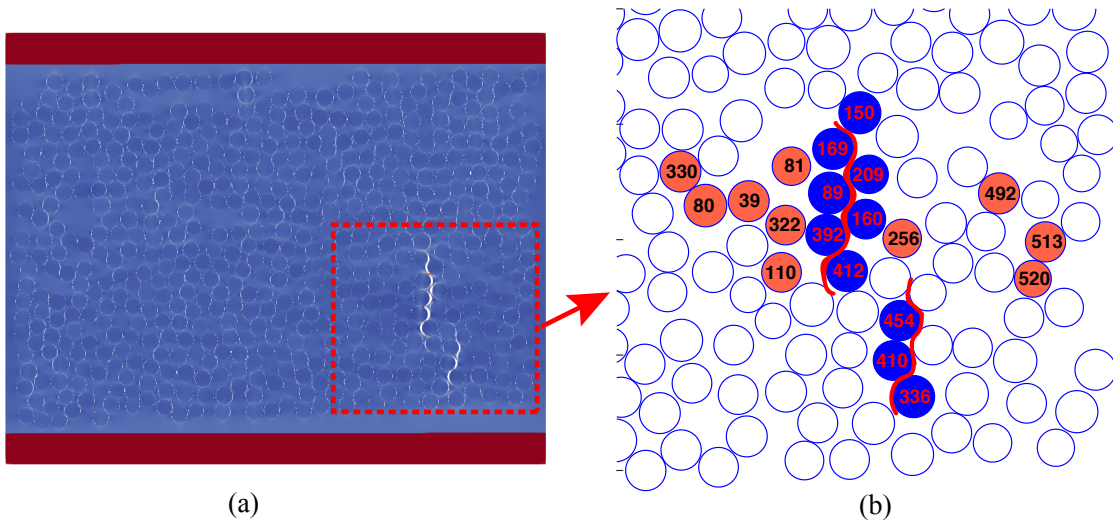


Figure 12: Location of the fibers with the ten most positive (orange) and ten most negative (blue) radius sensitivities associated with the formation of the first crack. The fibers are labeled according to the sensitivity curves shown in Fig. 11(c). The red curve in (b) indicates the crack path.

The significance of the sign of the sensitivities for this complex failure event is similar to that described earlier for the simpler two-fiber case: as transverse cracking takes place, the

transverse stress-strain response decreases (i.e., the shape sensitivity is negative) as the radius of the fibers involved in the failure event increases, while the unloading taking place primarily along interfaces immediately adjacent to the forming crack leads to a positive sensitivity of the transverse stress-strain curve for these fibers.

This competition between positive (cracking) and negative (unloading) sensitivities can be observed in Fig. 13, which presents the location of the fibers with the twenty largest (orange, positive) and smallest (blue, negative) sensitivities at four values of the applied strain during the formation of the first and the second transverse cracks. In the very initial stages, before any crack appears (Fig. 13(a)), the location of the fibers with the largest and smallest sensitivities is mostly random, although some of the fibers with the most negative radius sensitivity start to cluster around the location of the first crack. This trend continues until the first crack path becomes evident, and all the smallest sensitivities are associated with the fibers right along the crack path while the largest sensitivities cluster in the immediate vicinity of the crack path (Fig. 13(b)). As the crack further propagates, the smallest sensitivities follow the crack tip, while the sensitivities associated with the previously cracked region temporarily switch sign indicating unloading (Fig. 13(c)). As the second crack starts to initiate, the smallest sensitivities move to the second crack path, further unloading the fibers located along the first crack path (Fig. 13(d)).

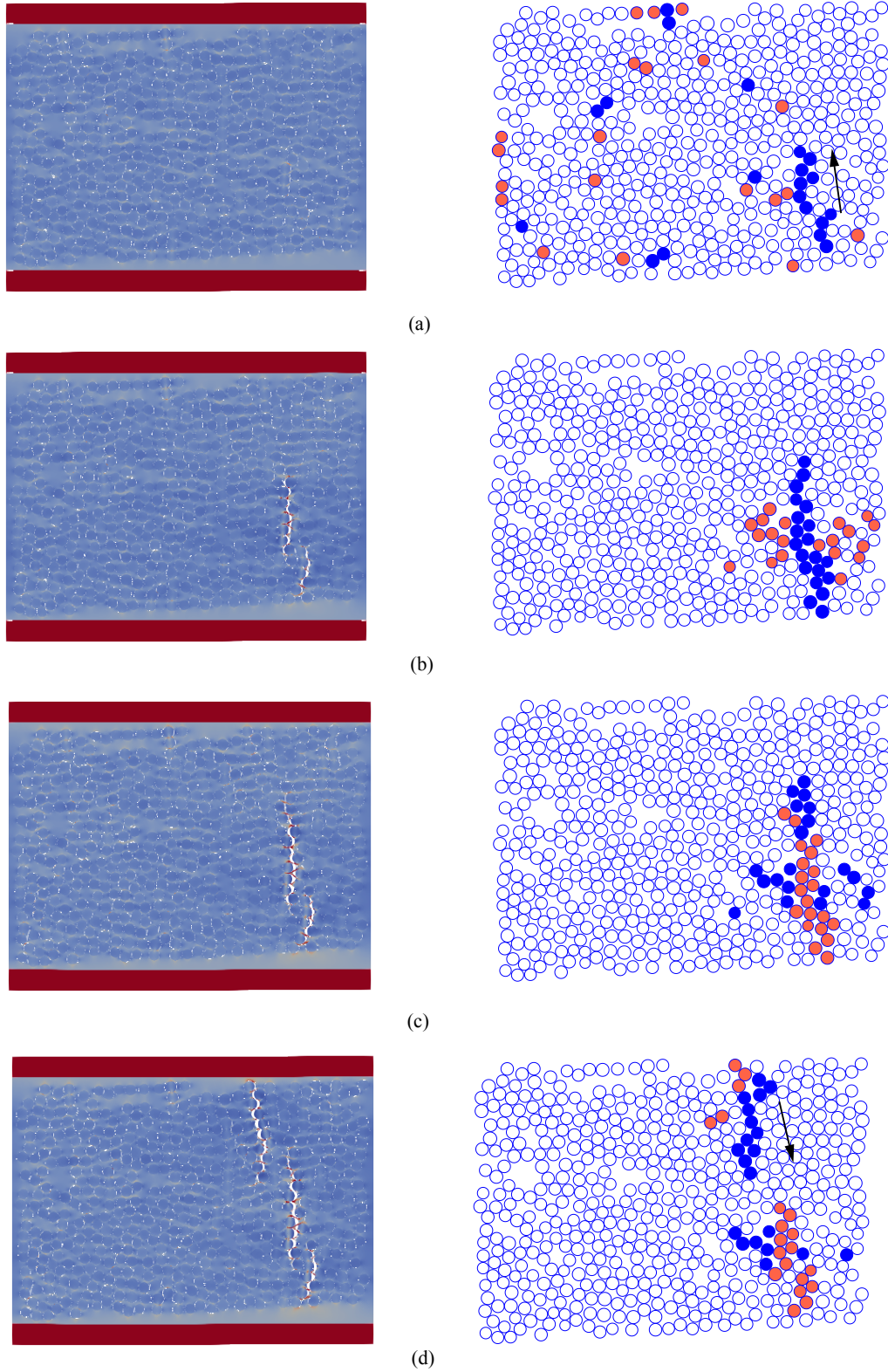


Figure 13: Evolution of deformed composite laminate (left figures) and location of the fibers with the largest (orange) and smallest (blue) radius sensitivities (right figures) during the formation of the first and second crack path at four values of the applied strain: (a) 0.78%; (b) 1.40%; (c) 1.45% and (d) 1.59%. The arrows indicate the crack propagation direction.

The sensitivities with respect to the mean ( $\mu_R$ ) and standard deviation ( $s_R$ ) of the fiber radii are shown in Fig. 14(a), with details on the initial part of the curves and on the strain values associated with the appearance of the first crack presented in Fig. 14(b) and (c), respectively. The initially positive values of the sensitivities with respect to both  $\mu_R$  and  $s_R$  indicate that increasing either the mean value or the standard deviation of the fiber radii increases the load bearing capability of the composites before failure initiates. However, at the appearance of the first crack, both  $\partial\bar{\sigma}/\partial\mu_R$  and  $\partial\bar{\sigma}/\partial s_R$  become negative, suggesting that the load bearing capacity of the composites at crack initiation would be increased by decreasing the mean and/or standard deviation of fiber radii.

The sensitivities with respect to the mean and standard deviation of the nearest-neighbor distance are presented in Fig. 14(d-f). The sensitivities  $\frac{\partial\bar{\sigma}}{\partial\mu_\delta}$  is -0.5 times  $\frac{\partial\bar{\sigma}}{\partial\mu_R}$  as noted earlier. As indicated in the figure, the sensitivity  $\frac{\partial\bar{\sigma}}{\partial\mu_R}$  is initially negative and becomes positive at the appearance of the first crack. This can be explained by the fact that increasing the mean nearest-neighbor distance while keeping the standard deviation of the nearest-neighbor distance fixed along the direction of  $\mathbf{v}_1 = [1, 1, \dots, 1]/\sqrt{n}$  is equivalent to decreasing the fiber radii uniformly. This uniform reduction of the fiber radii leads to a lower fiber volume fraction at the onset of loading, and thereby to a reduced stress magnitude, hence the negative sensitivity. At the initiation of the first crack, decreasing the fiber radii uniformly increases the nearest-distance between every fiber pair, thereby reducing the stress concentration and delaying the crack formation, hence the positive sensitivity.

When decreasing the standard deviation of nearest-neighbor distance while keeping mean nearest-neighbor distance fixed along the direction of  $\mathbf{v}_2 = [R_1 - \mu_R, R_2 - \mu_R, \dots, R_n - \mu_R]/\sqrt{\sum_{i=1}^n (R_i - \mu_R)^2}$ , the change in fiber radii and in nearest-distance depends on the specific configuration of each fiber pair. Therefore, the sensitivity of  $\bar{\sigma}$  with respect to  $s_\delta$  is microstructure specific. For the simulated microstructure, the sensitivities of  $\bar{\sigma}$  with respect to  $s_\delta$  shows a negative initial value, which indicates that increasing the standard deviation of nearest-neighbor distance decreases the transverse stress-strain curve before failure initiates. However, when the first crack initiates, the sensitivities become positive, indicating that decreasing the standard deviation of nearest-neighbor distance (while keeping  $\mu_\delta$  fixed) increases the load bearing capacity of the composites at crack initiation.

## 5 Summary

A sensitivity analysis of the transverse stress-strain response of a composite laminate with respect to the geometrical parameters as well as their distribution parameters has been presented. This method is based on the cohesive Interface-enriched Generalized Finite Element Method that utilizes  $C^{-1}$  continuous enrichment functions and a cohesive model to capture the transverse cracking due to fiber/matrix interface debonding. The sensitivity calculations have been implemented in a parallel IGFEM solver and verified through comparison with fi-

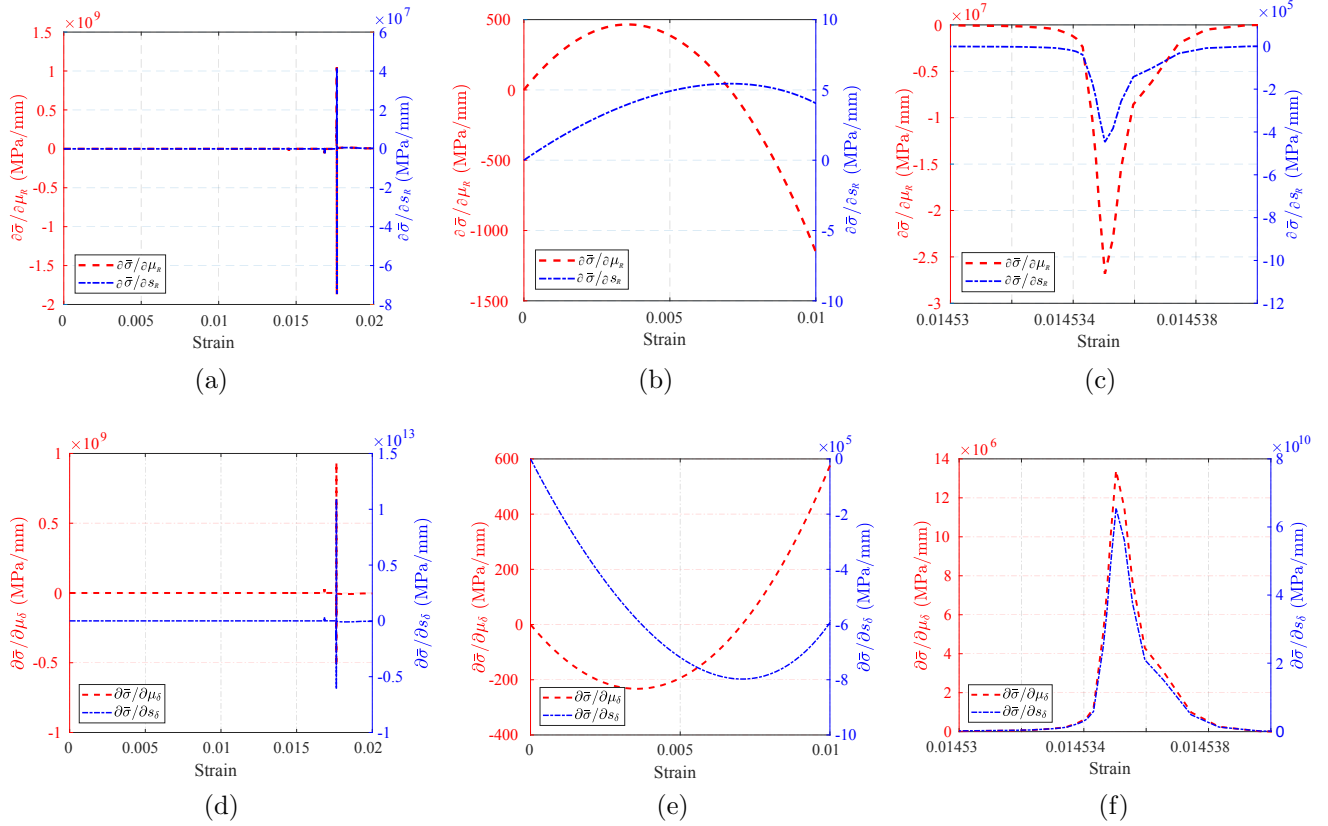


Figure 14: Top row: (a) Sensitivities of  $\bar{\sigma}$  with respect to the mean and standard deviation of the fiber radii, with (b) and (c) showing details on the initial portion of the curves and on the appearance of the first crack. Bottom row: similar sensitivity curves with respect to the mean and standard deviation of the nearest-neighbor distance distribution.

nite difference approximations. The sensitivity analysis has also been conducted on a realistic microstructure consisting of hundreds of fibers to understand the physical significance of the sensitivities. Beyond providing insight on the failure process itself, the sensitivity analysis may provide guidance for improving the transverse failure response of composite laminate by controlling the parameters defining the distribution parameters of fiber radii.

## 6 Acknowledgments

This work has been supported through Grant # FA9550-12-1-0445 to the Center of Excellence on Integrated Materials Modeling (CEIMM) at Johns Hopkins University (partners JHU, UIUC, UCSB), awarded by the AFOSR/RSL 290 (Computational Mathematics Program, Manager Dr. A. Sayir) and AFRL/RX (Monitors Dr. C. Woodward and Dr. C. Przybyla).

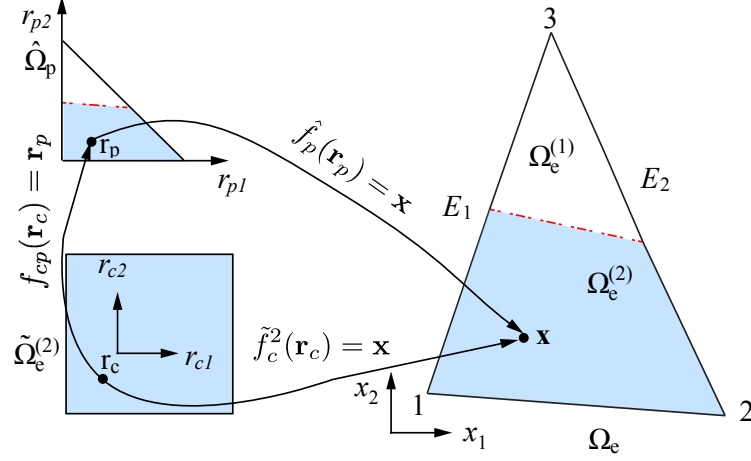


Figure 15: Mapping relates the master and integration elements with their isoparametric domains:  $\tilde{f}_c^{(2)}(\mathbf{r}_c)$  maps the isoparametric element  $\hat{\Omega}_e^{(2)}$  to the integration element  $\Omega_e^{(2)}$ ;  $\hat{f}_p(\mathbf{r}_p)$  maps the isoparametric element  $\hat{\Omega}_p$  to the master element  $\Omega_e$ ;  $f_{cp}(\mathbf{r}_p)$  is a composite mapping from  $\hat{\Omega}_e^{(2)}$  to  $\hat{\Omega}_p$ .

## Appendix A Derivation of the pseudo load

To perform the integration over the enriched elements, three different mappings are defined as proposed in Ref. [10]. These mappings relate the parent and children elements to their corresponding isoparameteric elements as shown in Fig. 15 by

$$\mathbf{x} = \tilde{f}_p(\mathbf{r}^p) = \sum_{n=1}^{M^p} N_n^p(\mathbf{r}^p) \mathbf{x}_n, \quad (\text{A1})$$

and

$$\mathbf{x} = \tilde{f}_c^{(k)}(\mathbf{r}^c) = \sum_{n=1}^{M^{c(k)}} N_n^{c(k)}(\mathbf{r}^c) \mathbf{x}_n, \quad (\text{A2})$$

where  $M^p$  and  $M^{c(k)}$  respectively denote the number of nodes in the master element and the  $k^{\text{th}}$  integration element, and  $N_n^p$  and  $N_n^{c(k)}$  are the corresponding shape functions.

In the master element, the material derivative of shape functions are expressed as

$$N_n^{p*} = \sum_{i=1}^{nsd} \frac{dN_n^p}{dx_i} \nabla_i, \quad (\text{A3})$$

where  $nsd$  denotes number of space dimension. Differentiating the above equation with respect to the spatial coordinates yields the expression of the components of  $\mathbf{B}^*$  appearing in Eq. (12) as

$$\frac{dN_n^{p*}}{d\mathbf{x}} = -\mathbf{J}^{p-1} \frac{d\mathbf{J}^p}{d\mathbf{d}} \mathbf{J}^{p-1} \frac{dN_n^p}{d\mathbf{r}^p} + \mathbf{J}^{p-1} \frac{d^2 N_n^p}{d\mathbf{r}^{p2}} \mathbf{J}^{p-1} \nabla, \quad (\text{A4})$$

in which  $\mathbf{J}^p$  is the Jacobian of the mapping  $\hat{f}_p(\mathbf{r}_p)$

$$J_{\alpha i}^p = \sum_{n=1}^{M^p} \frac{dN_n^p(\mathbf{r}^p)}{dr_\alpha^p} x_{ni}, \quad (\text{A5})$$

The sensitivity of  $\mathbf{J}^p$  with respect to the design variable  $\mathbf{d}$  is

$$\frac{dJ_{\alpha i}^p}{d\mathbf{d}} = \sum_{n=1}^{M^p} \frac{d^2 N_n^p}{dr_\alpha^p dr_\beta^p} J_{\beta j}^p x_{ni}. \quad (\text{A6})$$

In the integration elements, the material derivative of shape function vanishes:

$$N_n^{c(k)*} = 0. \quad (\text{A7})$$

Also,

$$\left( \frac{dN_n^{c(k)*}}{d\mathbf{x}} \right) = -\mathbf{J}^{c(k)-1} \frac{d\mathbf{J}^{c(k)}}{d\mathbf{d}} \mathbf{J}^{c(k)-1} \frac{dN_n^{c(k)}}{d\mathbf{r}^c}, \quad (\text{A8})$$

in which  $\mathbf{J}^c$  is the Jacobian of the mapping from the child element to the enriched element, similar to  $\mathbf{J}^p$ , defined as

$$J_{\alpha i}^c = \sum_{n=1}^{M^c} \frac{dN_n^c(\mathbf{r}^c)}{dr_\alpha^c} x_{ni}. \quad (\text{A9})$$

Similarly, the sensitivity of  $\mathbf{J}^c$  is given by

$$\frac{dJ_{\alpha i}^{c(k)}}{d\mathbf{d}} = \sum_{n=1}^{M^c} \frac{dN_n^{c(k)}(r^c)}{dr_\alpha^c} \mathbb{V}_{ni}. \quad (\text{A10})$$

The shape velocity is only computed in the integration elements as

$$\mathbb{V}_i = \sum_{n=1}^{M^{c(k)}} N_n^c(r^c) \mathbb{V}_{ni}. \quad (\text{A11})$$

The divergence of shape velocity is given by

$$\text{div}(\mathbb{V}) = \sum_{i=1}^{nsd} \sum_{n=1}^{M^{c(k)}} \frac{dN_n^{c(k)}}{dx_i} \mathbb{V}_{ni}. \quad (\text{A12})$$

For the interface elements shown in Fig. 16, the rotation matrix used to link the local and global coordinate systems takes the form of

$$\mathbf{R}_c = \begin{bmatrix} \cos\theta & \sin\theta \\ -\sin\theta & \cos\theta \end{bmatrix}, \quad (\text{A13})$$

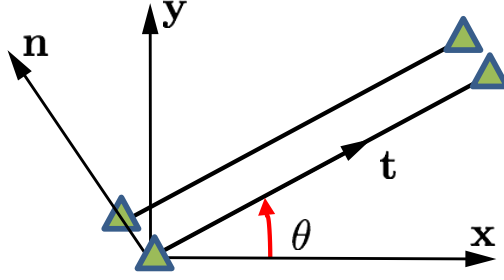


Figure 16: Local coordinates of the interface elements.

which leads to

$$\mathbf{B}_c^* = \mathbf{R}_c^* \mathbf{N}_c = \begin{bmatrix} -\sin\theta & \cos\theta \\ -\cos\theta & -\sin\theta \end{bmatrix} \frac{d\theta}{d\mathbf{d}} \mathbf{N}_c. \quad (\text{A14})$$

The derivative of the angle  $\theta$  with respect to geometric parameters is derived as

$$\frac{d\theta}{d\mathbf{d}} = \cos^2\theta (J_{11} \frac{dJ_{12}}{d\mathbf{d}} - J_{12} \frac{dJ_{11}}{d\mathbf{d}}) / J_{11}^2, \quad (\text{A15})$$

where

$$J_{\alpha i} = \sum_{n=1}^n \frac{dN_n(r)}{dr_\alpha} x_{ni}, \quad (\text{A16})$$

and

$$\frac{dJ_{\alpha i}}{d\mathbf{d}} = \sum_{n=1}^n \frac{dN_n(r)}{dr_\alpha} \mathbb{V}_{ni}. \quad (\text{A17})$$

The contour divergence of shape velocity is given by

$$\text{div}_\Gamma(\mathbb{V}) = \sum_{i=1}^{nsd} \sum_{n=1}^{M^t} \frac{dN_n^t}{dx_i} \mathbb{V}_{ni}, \quad (\text{A18})$$

where  $M^t$  is equal to the number of nodes of the base of the cohesive element ( $M^t = 3$  for the cohesive elements in Fig. 16), and  $N^t$  denotes the shape function.

## Appendix B Choice for the direction $\mathbf{v}$

Moments are used to characterize the central tendency of a set of data ( $\mathbf{x} = (x_1, x_2, \dots, x_n)$ ) clustering around some particular value. The first- to fourth-order moments correspond to the mean ( $\mu_x$ ), variance (Var), skewness (Skew) and kurtosis (Kurt), respectively. They are defined as

$$\mu_x = \frac{1}{n} \sum_{j=1}^n x_j, \quad (\text{A19})$$

$$\text{Var}(\mathbf{x}) = \frac{1}{n-1} \sum_{j=1}^n (x_j - \mu_x)^2, \quad (\text{A20})$$

$$\text{Skew}(\mathbf{x}) = \frac{1}{n} \sum_{j=1}^n \left[ \frac{x_j - \mu_x}{s_x} \right]^3, \quad (\text{A21})$$

and

$$\text{Kurt}(\mathbf{x}) = \frac{1}{n} \sum_{j=1}^n \left[ \frac{x_j - \mu_x}{s_x} \right]^4 - 3. \quad (\text{A22})$$

The term  $-3$  in Eq. (A22) is introduced to make the value vanish for a normal distribution. We can generalize the moment definition up to  $n$ -th order as

$$M_i(\mathbf{x}) = \frac{1}{n} \sum_{j=1}^n \left[ \frac{x_j - \mu_x}{s_x} \right]^i - \beta_i; i = 3, 4, \dots, n, \quad (\text{A23})$$

where  $\beta_i$  is introduced to make the value zero for a normal distribution, similar to Eq. (A22). It also should be noted that the expression of the generalized moment starts from the third order since the second-order moment (i.e., the variance) has a coefficient of  $\frac{1}{n-1}$  rather than  $\frac{1}{n}$ .

In the case of a two-fiber microstructure, if we require the standard deviation to be constant while increasing the mean by  $\alpha\mu_R$  by altering  $\mathbf{R} = (R_1, R_2)$  in the direction  $\mathbf{v} = (v_1, v_2)$ , we have

$$\begin{cases} \frac{R_1 + R_2 + v_1 + v_2}{2} = (1 + \alpha) \frac{R_1 + R_2}{2}, \\ (R_1 + v_1 - (1 + \alpha)\mu_R)^2 + (R_2 + v_2 - (1 + \alpha)\mu_R)^2 = (R_1 - \mu_R)^2 + (R_2 - \mu_R)^2, \end{cases} \quad (\text{A24})$$

which yields the solution  $\mathbf{v} = \alpha\mu_R[1, 1]$ . In other words, altering  $\mathbf{R}$  along the direction of  $\mathbf{v} = [1, 1]/\sqrt{2}$  will keep the standard deviation constant while changing the mean.

On the other hand, if we require the mean to be constant while increasing the standard deviation by  $\eta s_R$  by perturbing  $\mathbf{R} = (R_1, R_2)$  in the direction  $\mathbf{v}$ , we have:

$$\begin{cases} \mu_R = \frac{R_1 + R_2 + v_1 + v_2}{2} = \frac{R_1 + R_2}{2}, \\ (R_1 + v_1 - \mu_R)^2 + (R_2 + v_2 - \mu_R)^2 = (1 + \eta)^2 \left[ (R_1 - \mu_R)^2 + (R_2 - \mu_R)^2 \right], \end{cases} \quad (\text{A25})$$

from which we get  $\mathbf{v} = \frac{\eta}{2}[R_1 - R_2, R_2 - R_1] = \eta[R_1 - \mu_R, R_2 - \mu_R]$ .

Now let us consider the case of a microstructure with  $n$  fibers ( $n \geq 3$ ). Increasing the mean by  $\alpha\mu_R$  while keeping all other moment (up to  $n$ -th order) fixed by perturbing  $\mathbf{R} =$

$(R_1, R_2, \dots, R_n)$  in direction  $\mathbf{v}$  yields:

$$\begin{cases} \sum_{i=1}^n (R_i + v_i)/n = (1 + \alpha) \sum_{i=1}^n R_i/n = (1 + \alpha)\mu_R, \\ s_R = \sum_{i=1}^n \left( R_i + v_i - (1 + \alpha)\mu_R \right)^2 = \sum_{i=1}^n \left( R_i - \mu_R \right)^2, \\ M_j = \sum_{i=1}^n \left( \frac{R_i + v_i - (1 + \alpha)\mu_R}{s_R} \right)^j = \sum_{i=1}^n \left( \frac{R_i - \mu_R}{s_R} \right)^j; \quad j = 3, 4, \dots, n. \end{cases} \quad (\text{A26})$$

The system of equation described by Eq. (A26) has multiple solutions. One can readily show that  $\mathbf{v} = \alpha\mu_R[1, 1, \dots, 1]$  is a solution, indicating that changing  $\mathbf{R}$  along the direction  $\mathbf{v} = [1, 1, \dots, 1]/\sqrt{n}$  will modify the mean while maintaining all other moments up to  $n$ -th order fixed.

Similarly, changing the standard deviation to  $(1 + \eta)s_R$  while keeping the mean and all higher moments fixed leads to

$$\begin{cases} \mu_R = \sum_{i=1}^n (R_i + v_i)/n = \sum_{i=1}^n R_i/n, \\ \frac{1}{2} \sum_{i=1}^n \left( R_i + v_i - \mu_R \right)^2 = \frac{(1 + \eta)^2}{2} \sum_{i=1}^n \left( R_i - \mu_R \right)^2 = (1 + \eta)^2 s_R^2, \\ M_j = \sum_{i=1}^n \left( \frac{R_i + v_i - \mu_R}{(1 + \eta)s_R} \right)^j = \sum_{i=1}^n \left( \frac{R_i - \mu_R}{(1 + \eta)s_R} \right)^j; \quad j = 3, 4, \dots, n, \end{cases} \quad (\text{A27})$$

which has a solution  $\mathbf{v} = \eta[R_1 - \mu_R, R_2 - \mu_R, \dots, R_n - \mu_R]$ .

## References

- [1] S. Soghrati and P. H. Geubelle. A 3D interface-enriched generalized finite element method for weakly discontinuous problems with complex internal geometries. *Comput. Methods Appl. Mech. Eng.*, 217:46–57, 2012.
- [2] M. Safdari, A. R. Najafi, Nancy R. Sottos, and P. H. Geubelle. A nurbs-based generalized finite element scheme for 3d simulation of heterogeneous materials. *J. Comput. Phys.*, 318:373–390, 2016.
- [3] M. H.Y. Tan, M. Safdari, A. R. Najafi, and P. H. Geubelle. A nurbs-based interface-enriched generalized finite element scheme for the thermal analysis and design of microvascular composites. *Comput. Methods Appl. Mech. Eng.*, 283:1382–1400, 2015.
- [4] K. Zhang, J. Jin, and P. H. Geubelle. A 3-d interface-enriched generalized fem for electromagnetic problems with nonconformal discretizations. *IEEE Trans. Antennas Propag.*, 63:5637–5649, 2015.
- [5] M. H.Y. Tan, A. R. Najafi, S. J. Pety, S. R. White, and P.H. Geubelle. Gradient-based design of actively-cooled microvascular composite panels. *Int. J. Heat Mass Transfer*, 103: 594–606, 2016.
- [6] M. H. Y. Tan and P. H. Geubelle. 3D dimensionally reduced modeling and gradient-based optimization of microchannel cooling networks. *Comput. Methods Appl. Mech. Eng.*, 323: 230–249, 2017.
- [7] S. J. Pety, M. H. Y. Tan, A. R. Najafi, P. R. Barnett, P. H. Geubelle, and S. R. White. Carbon fiber composites with 2D microvascular networks for battery cooling. *Int. J. Heat Mass Transfer*, 115:513–522, 2017.
- [8] M. H.Y. Tan, A. R. Najafi, S. J. Pety, S. R. White, and P. H. Geubelle. Multi-objective design of microvascular panels for battery cooling applications. *Appl. Therm. Eng.*, 2018.
- [9] M. H. Y. Tan, D. Bunce, A. R. M. Ghosh, and P. H. Geubelle. Computational design of microvascular radiative cooling panels for nanosatellites. *J. Thermophysics Heat Tr.*, 32: 605–616, 2018.
- [10] A. R Najafi, M. Safdari, D. A. Tortorelli, and P. H. Geubelle. A gradient-based shape optimization scheme using an interface-enriched generalized FEM. *Comput. Methods Appl. Mech. Eng.*, 296:1–17, 2015.
- [11] A. R. Najafi, M. Safdari, D. A. Tortorelli, and P. H. Geubelle. Shape optimization using a nurbs-based interface-enriched generalized fem. *Int. J. Numer. Methods Eng.*, 2017.

- [12] K. W. Garrett and J. E. Bailey. The effect of resin failure strain on the tensile properties of glass fibre-reinforced polyester cross-ply laminates. *J. Mater. Sci.*, 12:2189–2194, 1977.
- [13] J. A. Nairn. Matrix microcracking in composites. In Taljara–Man-son, editor, *Polymer Matrix Composites*. Elsevier Science, 2000.
- [14] I. M. Daniel and O. Ishai. *Engineering Mechanics of Composite Materials*. Oxford University Press, 2005. 2nd edition.
- [15] L. P. Canal, J. Segurado, and J. LLorca. Failure surface of epoxy-modified fiber-reinforced composites under transverse tension and out-of-plane shear. *Int. J. Solids Struct.*, 46(11):2265–2274, 2009.
- [16] T. J. Vaughan and C. T. McCarthy. Micromechanical modelling of the transverse damage behaviour in fibre reinforced composites. *Compos. Sci. Technol.*, 71:388–396, 2011.
- [17] V. I. Kushch, S. V. Shmegeera, P. Brondsted, and L. Mishnaevsky. Numerical simulation of progressive debonding in fiber reinforced composite under transverse loading. *Int J Eng Sci*, 49:17–29, 2011.
- [18] H. Tan, C. Liu, Y. Huang, and P. H. Geubelle. The cohesive law for the particle/matrix interfaces in high explosives. *J. Mech. Phys. Solids*, 53(8):1892–1917, 2005.
- [19] V. Dantuluri, S. Maiti, P. H. Geubelle, R. Patel, and H. Kilic. Cohesive modeling of delamination in Z-pin reinforced composite laminates. *Compos. Sci. Technol.*, 67:616–631, 2007.
- [20] V.-T. Phan, X. Zhang, Y. Li, and C. Oskay. Microscale modeling of creep deformation and rupture in nickel-based superalloy in 617 at high temperature. *Mech. Mater.*, 114:215–227, 2017.
- [21] R. Hu, C. Prakash, V. Tomar, M. Harr, I. E. Gunduz, and C. Oskay. Experimentally-validated mesoscale modeling of the coupled mechanical-thermal response of AP-HTPB energetic material under dynamic loading. *Int. J. Fracture*, 203:277–298, 2017.
- [22] C.B. Montgomery. *Multiscale Characterization of Carbon Fiber-Reinforced Epoxy Composites*. dissertation, University of Illinois at Urbana-Champaign, 2018.
- [23] A. M. Aragon and A. Simone. The discontinuity-enriched finite element method. *Int. J. Numer. Methods Eng.*, 112:1589–1613, 2017.
- [24] D. Brandyberry and P. H. Geubelle. Multiscale Sensitivity Analysis of Failure in Composite Materials Using an Interface-Enriched Generalized FEM. In Yu W., Pipes R.B., and Goodsell J., editors, *32nd Technical Conference of the American Society for Composites*

- 2017, volume 2, pages 1044–1056, West Lafayette, IN, oct 2017. DEStech Publications, Inc.
- [25] S. Zacek. Exploring the link between microstructure statistics and transverse ply fracture in carbon/epoxy composites. Master’s thesis, University of Illinois at Urbana-Champaign, US, 2017.
- [26] S. Zacek, D. Brandyberry, A. Klepacki, C. Montgomery, M. Shakiba, M. Rossol, A. Najafi, X. Zhang, N. Sottos, P. H. Geubelle, C. Przybyla, and G. Jefferson. Transverse failure of unidirectional composites: Sensitivity to interfacial properties. *Submitted.*, 2018.
- [27] M. Shakiba, D. Brandyberry, S. Zacek, and P. H. Geubelle. Transverse failure of carbon fiber composites: Analytical sensitivity with respect to the distribution of fiber/matrix interface properties. *In revision.*, 2019.
- [28] M. Ortiz and A. Pandolfi. Finite-deformation irreversible cohesive elements for three-dimensional crack-propagation analysis. *Int. J. Numer. Methods Eng.*, 44:1267–1282, 1999.
- [29] P. H. Geubelle M. G. Kulkarni and K. Matous. Multi-scale modeling of heterogeneous adhesives: Effect of particle decohesion. *Mech. Mater.*, 41:573 – 583, 2009.
- [30] P. Geubelle. D. Brandyberry, M. Safdari. *Par-IGFEM User’s Manual*, 2018.
- [31] S. Balay, S. Abhyankar, M. F. Adams, J. B., P. Brune, K. Buschelman, L. Dalcin, A. Dener, V. Eijkhout, W. D. Gropp, D. Kaushik, M. G. Knepley, D. A. May, L. Curfman McInnes, R. T. Mills, T. Munson, K. Rupp, P. Sanan, B. F. Smith, S. Zampini, H. Zhang, and H. Zhang. PETSc Web page. <http://www.mcs.anl.gov/petsc>, 2018.
- [32] K. J. Bathe and A. P. Cimento. Some practical procedures for the solution of nonlinear finite element equations. *Comput. Methods Appl. Mech. Eng.*, 22:59–85, 1980.
- [33] Y. F. Gao and A. F. Bower. A simple technique for avoiding convergence problems in finite element simulations of crack nucleation and growth on cohesive interfaces. *Modelling Simul. Mater. Sci. Eng*, 12:453–463, 2004.
- [34] J. C. Halpin and J. L. Kardos. The Halpin-Tsai equations: A review. *Polym. Eng. Sci.*, 16:344–352, 1976.